Computers in Biology and Medicine 129 (2021) 104168

Contents lists available at ScienceDirect

Computers in Biology and Medicine

journal homepage: http://www.elsevier.com/locate/compbiomed

# Apparent growth tensor of left ventricular post myocardial infarction – In human first natural history study

Wenguang Li [a], Hao Gao [b], Kenneth Mangion [c], Colin Berry [c], Xiaoyu Luo [b,*]

[a] School of Engineering, University of Glasgow, UK
[b] School of Mathematics and Statistics, University of Glasgow, UK
[c] College of Medical, Veterinary and Life Sciences, University of Glasgow, UK

ARTICLE INFO

*Keywords:*
Left ventricle
Myocardial infarction
Continuum mechanics
Growth and remodelling
Growth tensor
Cardiac magnetic resonance imaging

ABSTRACT

An outstanding challenge in modelling biomechanics after myocardial infarction (MI) is to estimate the so-called growth tensor. Since it is impossible to track pure growth induced geometry change from in vivo magnetic resonance images alone, in this work, we propose a way of estimating a surrogate or apparent growth tensor of the human left ventricle using cine magnetic resonance (CMR) and late gadolinium enhanced (LGE) images of 16 patients following acute MI. The apparent growth tensor is evaluated at four time-points following myocardial reperfusion: 4–12 h (baseline), 3 days, 10 days and 7 months. We have identified three different growth patterns classified as the *Dilation, No-Change* and *Shrinkage* groups defined by the left ventricle end-diastole cavity volume change from baseline. We study the- trends in both the infarct and remote regions. Importantly, although the *No-Change* group has little change in the ventricular cavity volume, significant remodelling changes are seen within the myocardial wall, both in the infarct and remote regions. Through statistical analysis, we show that the growth tensor invariants can be used as effective biomarkers for adverse and favourable remodelling of the heart from 10 days onwards post-MI with statistically significant changes over time, in contrast to most of the routine clinical indices. We believe this is the first time that the apparent growth tensor has been estimated from in vivo CMR images post-MI. Our study not only provides much-needed information for understanding growth and remodelling in the human heart following acute MI, but also identifies novel biomarker for assessing heart disease progression.

## 1. Introduction

Myocardial infarction (MI), also known as heart attack, involves cardiomyocyte death following the loss of antegrade coronary blood flow. After acute MI, the left ventricle (LV) undergoes a sequence of adaptations in structure and function, regulated by mechanical, neurohormonal and genetic factors [7,17,47]. This myocardium growth & remodelling (G&R) may become maladaptive. The LV may experience dilation in association with wall thinning around the infarct zone, and hypertrophy or fibrosis (collagen fibre scar) in the remote zone. Adverse G&R, i.e. dila-tion, can lead to heart failure, a major source of morbidity and mortality [16], and sudden cardiac death due to malignant arrhythmias. Over the years, with improvement in the treatment of acute MI, more people are surviving post-MI, but with a subsequent rise in heart failure [42,51].

Cardiac G&R has previously been categorized into two types: (1) concentric G&R with wall thickening caused by pressure over-loading; (2) eccentric G&R with dilation of the ventricular cavity and wall stretching, both induced by pressure over-loading [3,24]. However, MI-induced LV G&R is more complex, and recently a classification, such as reverse remodelling, no remodelling, and adverse remodelling, was proposed in terms of 12% relative changes in LV end-diastolic volume (LVEDV) [11]. MI-induced progressive G&R is an important clinical determinant of heart failure [30], and arresting or prompting reverse remodelling is a long-term aim to reduce the risk of heart failure [7].

Usually, LV G&R is quantified by evaluating LV global changes, such as LVEDV, end-systolic volume (ESV), ejection fraction (EF) and wall thickness [10]. However, these indices only describe an incomplete picture of the G&R process. More detailed local patterns of G&R in MI patients, the difference in MI and remote regions can provide additional

* Corresponding author.
*E-mail addresses:* wenguang.li@glasgow.ac.uk (W. Li), Hao.Gao@glasgow.ac.uk (H. Gao), Kenneth.Mangion@glasgow.ac.uk (K. Mangion), Colin.Berry@glasgow.ac.uk (C. Berry), Xiaoyu.Luo@glasgow.ac.uk (X. Luo).

https://doi.org/10.1016/j.compbiomed.2020.104168
Received 24 August 2020; Received in revised form 3 December 2020; Accepted 3 December 2020
Available online 9 December 2020

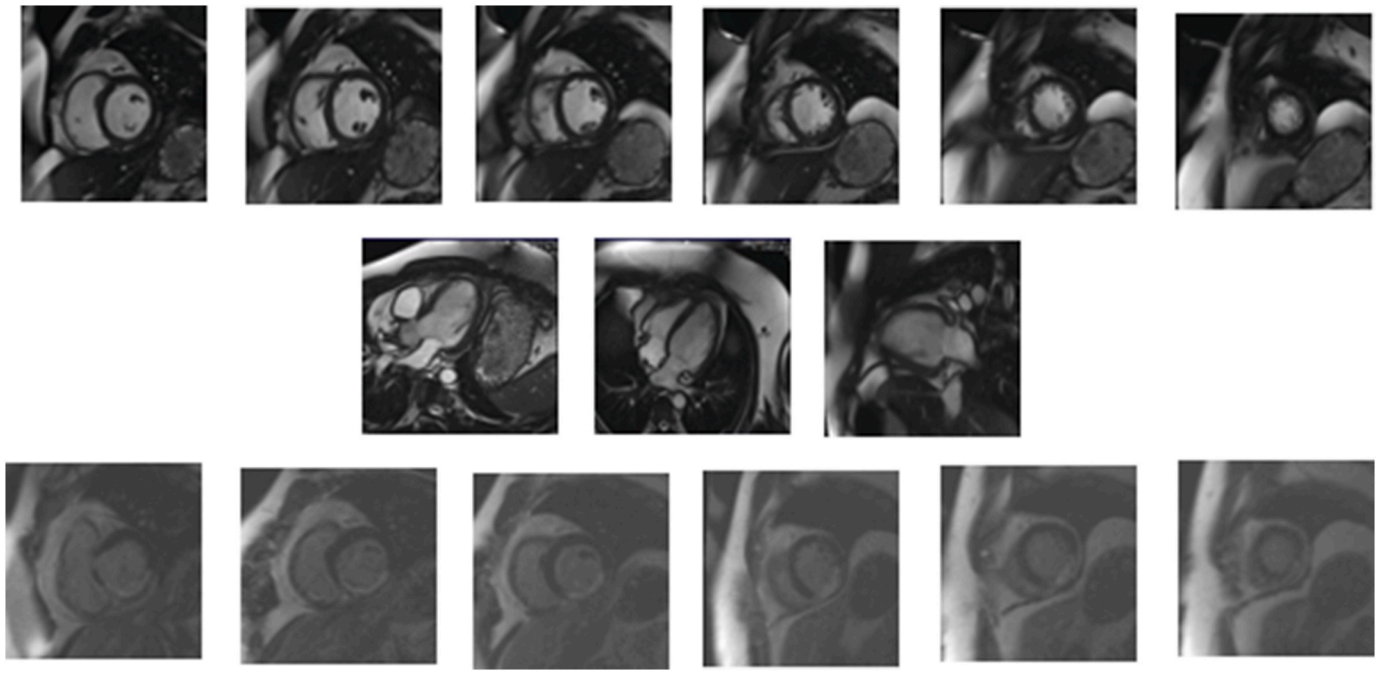

**Fig. 1.** Acquired CMR images of a typical patient at acute-MI. Top row: short-axis cine images at end-diastole from the base to the apex. Middle row: long-axis cine images at end-diastole at LVOT, HLA and VLA planes. Bottom row: short-axis LGE images at mid-diastole from the base to the apex.

insights into identifying patients with a high risk of adverse remodelling and evaluating interventions aimed at reducing the progression of heart failure.

Quantification of local LV G&R following MI is difficult, requiring serial measurements of in vivo myocardium geometry and motion. For research purposes, measurements are often made in animals by tracking several small-sized beads embedded in the LV wall through open-chest surgery [26,27,39,49]. For example, Kass et al. [27] measured disproportionate epicardial dilation after transmural infarction of the canine LV within 7 days of acute MI. By suturing stainless steel spherical beads to the epicardial surface, they found that 1-h after infarction, the end-diastole area in the infarct region increased by 20.3% above healthy control (normal LV before infarction) compared with a 7.9% increase in the remote region. 24-hour post-MI, both the regions expanded by an additional 10%. One-week post-MI, the end-diastole area in the infarct region increased to 31.4% above the control, but the remote area became to only 8.5% above the control. Holmes et al. [26] measured scar transmural remodelling after infarction in five porcine hearts. Fitting the measured bead positions into a finite element (FE) model at 1- and 3-week post-MI, they calculated the post-MI strain against the reference configuration (at end-diastole before infarction). Their results showed that at 1-week post-MI, infarct expansion dominated the remodelling process, as characterized by the circumferential and longitudinal in-plane stretch and wall thinning. However, post-MI strain at 3-week is much more complex. Two out of five LVs showed continuous in-plane infarction expansion with wall-thinning, and the remaining three had in-plane shrinkage either with wall thinning or thickening. In a more recent study, Tsamis et al. [49] implanted three transmural columns of bead sets across the mid-lateral equatorial region of a sheep LV and recorded the bead positions using biplane cine-radiography before infarction and 7-week post-MI. They calculated the end-diastolic and end-systolic post-MI strains in a lateral-equatorial region adjacent to infarct by fitting bead positions using a FE model and found there were chronic muscle fibre lengthening ($>$ 10%) in the longitudinal direction, 25% shrinkage in the radial or transmural directions, and 15% decrease in the ventricular volume.

Although animal experiments can provide useful data for calibrating, validating and verifying various cardiac growth modelling theories, the bead implantation method is invasive and not suitable for human subjects. With the development of cardiac magnetic resonance (CMR) [5,6,15,54] and ultrasound imaging [45,46], it is now possible to quantify some regional geometry and function post-MI in vivo. However, using in vivo CMR images to track G&R post-MI is challenging. Longitudinal 3D cine images may not be available, motion artefacts may affect in the images, and ventricular geometries at different time-points must be co-registered. O'Regan et al. [40] studied LV remodelling during the first year after reperfused acute ST-elevation MI (STEMI) in 47 patients using a three-dimensional (3D) co-registration approach. Both short-axis cine and late gadolinium enhanced (LGE) images were co-registered to an atlas template and local expansion of the heart wall was tracked by using intensity-based similarities. End-diastolic remodelling is defined as the mean change of vertex separations from the matched endocardial and epicardial surfaces. Their results showed that in-plane expansion in the infarct region is greater than in the remote myocardium (1.6%$\pm$1.0 vs 0.3%$\pm$0.9), and associated with wall-thinning in the infarct region but no changes in wall thickness in the remote region. Additionally, they demonstrated that MI transmurality and microvascular obstruction (MVO) may affect local remodelling considerably. To our knowledge, O'Regan et al. [40] were the first group to report patient measurements of MI-induced local myocardial remodelling in vivo. However, they only studied the local expansion characterization and did not estimate the growth tensor.

Understanding G&R of the LV post-MI is critically important to risk stratifying preventive therapy for heart failure. A key element of monitoring a diseased heart is to extract growth tensor evolution with time from non-invasive clinical images. Computational models based on continuum mechanics and clinical imaging assessment techniques have recently been developed to overcome the limitations by describing G&R based on routine clinical images [2,9,55,56].

In this work, to quantify G&R in patients with recent MI and evaluate its relation to adverse remodelling, a continuum mechanics approach is employed to evaluate the LV apparent growth tensor in 16 patients post-MI undergoing CMR at 4 distinct time-points: at 4–12 h (baseline), 3 days, 10 days, and 7 months after reperfusion. Primary percutaneous coronary intervention (PPCI) was performed within a few hours ($<$*12* h) following the onset of acute MI. The end-diastolic (ED) LV geometries

**Table 1**
Patient information, where the symbols are defined as: A-Anterior, I-inferior, and S-septal, LCX: left circumflex artery, RCA: right coronary artery, LAD: left anterior descending artery, SBP: systolic blood pressure, DBP, diastolic blood pressure, MVO: Microvascular obstruction.

| Patient No | Gender | Age | Weight | Heart rate | SBP | DBP | MI size (%LV mass) | Cuplrit artery | MVO extent | LVEF acute | LVEF follow-up |
|---|---|---|---|---|---|---|---|---|---|---|---|
| 1 | Male | 64 | 99 | 61 | 151 | 97 | 7.1/I | LCX | 1.25 | 63.3 | 63.0 |
| 2 | Male | 53 | 78 | 65 | 102 | 64 | 15.4/S + I | RCA | 2.74 | 56.4 | 56.4 |
| 3 | Male | 60 | 104 | 104 | 117 | 86 | 16.0/A | RCA | 0.00 | 49.1 | 61.3 |
| 4 | Male | 33 | 94 | 105 | 152 | 94 | 28.4/A | LCX | 2.55 | 47.0 | 58.8 |
| 5 | Male | 60 | 61 | 65 | 155 | 77 | 5.2/S + I | RCA | 0.00 | 69.7 | 64.7 |
| 6 | Female | 63 | 70 | 91 | 156 | 97 | 29.9/S | LAD | 6.96 | 49.4 | 60.8 |
| 7 | Male | 54 | 85 | 77 | 136 | 86 | 36.4/S + I | LCX | 11.10 | 34.1 | 38.1 |
| 8 | Male | 61 | 99 | 54 | 104 | 68 | 13.2/S + I | RCA | 5.26 | 77.8 | 71.0 |
| 9 | Male | 35 | 127 | 97 | 126 | 85 | 11.5/S + I | RCA | 0.00 | 51.5 | 49.6 |
| 10 | Male | 43 | 76 | 78 | 130 | 76 | 23.2/S + I | RCA | 7.16 | 58.8 | 71.4 |
| 11 | Male | 61 | 83 | 47 | 155 | 95 | 3.6/S | RCA | 0.00 | 71.6 | 55.0 |
| 12 | Male | 61 | 86 | 66 | 154 | 84 | 43.3/S | LAD | 12.09 | 45.2 | 47.8 |
| 13 | Male | 58 | 90 | 73 | 185 | 82 | 17.2/A | LCX | 0.00 | 57.3 | 68.9 |
| 14 | Female | 58 | 47 | 76 | 129 | 71 | 32.3/I | LCX | 9.06 | 55.4 | 58.0 |
| 15 | Male | 62 | 86 | 89 | 166 | 94 | 2.5/A | LCX | 0.00 | 51.4 | 74.0 |
| 16 | Male | 63 | 84 | 76 | 127 | 88 | 9.1/S | LAD | 0.00 | 54.8 | 70.2 |

are first reconstructed based on CMR cine images at different time points. The MI regions are then delineated from corresponding short-axial LGE images. The reconstructed LV geometries are co-registered to a template LV finite element mesh, and the apparent growth tensors at end-diastole in MI and remote regions are calculated against the baseline LV geometry. All patients are further classified into three groups (Dilation, Shrinkage or No-Change) according to their end-diastolic volume changes based on the criteria proposed by Bulluck et al. [11] for adverse remodelling, reverse remodelling and no-remodelling behaviours. Finally, the invariants of the growth tensor extracted in both the MI and remote regions are investigated and their statistical significance is examined against the short-term (one week) and long-term (6 months) pump function recovery in these groups. We believe the outcomes of this study will be useful to quantitatively characterize G&R for patients post-MI, and provide much needed clinical input for mechanobiology modelling of G&R process in the human heart.

## 2. Methods

### 2.1. Patient population and CMR protocol

This study involves 16 STEMI patients with four longitudinal CMR scans, at 4–12 h, 3 days, 10 days, and 7 months after reperfusion. All patients were enrolled between May 2011 to November 2012 with acute STEMI (Clinical trial registration no, NCT 02072850). All patients provided written informed consent.

CMR imaging was performed on a Siemens MAGNETOM Avanto 1.5-T scanner (Erlangen, Germany) using an anterior phased-array body coil (12-element) and a posterior phased-array spine coil (24-element). A steady-state free precession sequence was used for LV structure and functional assessment (the cine images), consisting of a short-axis stack with slices of 7 mm thickness and 3 mm gap in-between, and three long-axis images: the horizontal long-axis (HLA), the vertical long-axis (VLA) and the left ventricular outflow tract (LVOT). Typical image parameters were repetition time: 3.3 ms, echo time: 1.2 ms, flip angle: 80°,

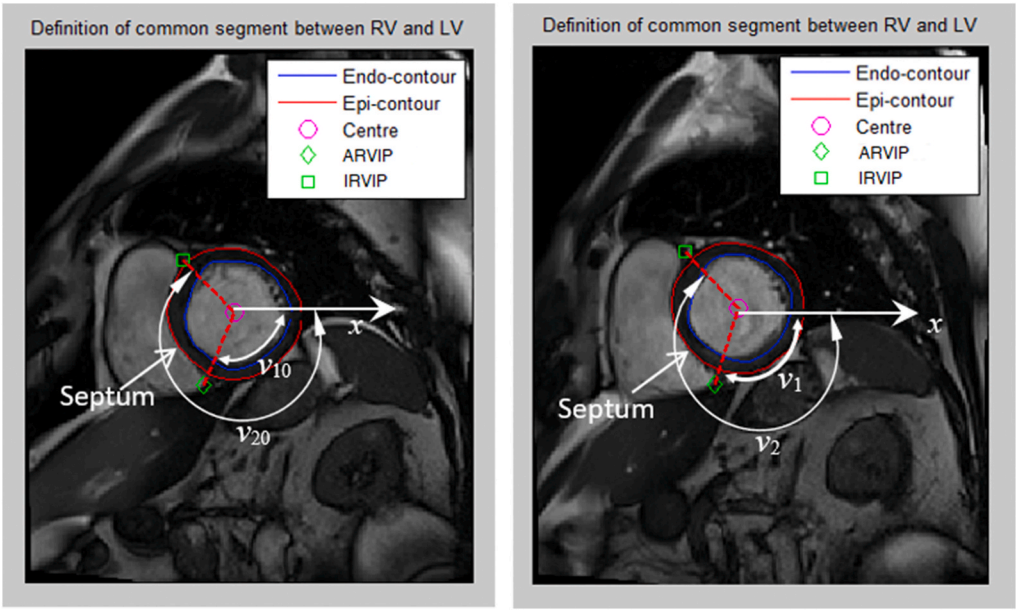


**Fig. 2.** To co-register the circumferential cross-sections of the LV at different scans, the septum is defined by $\nu_{20} - \nu_{10}$ at acute-state (baseline) and $\nu_2 - \nu_1$ at a later scan, guided by the right ventricular insertion points. The septum is between the ARVIP-anterior right ventricular insertion point and IRVIP-inferior right ventricular insertion point, discretized with the same number of hexahedral elements at all times.

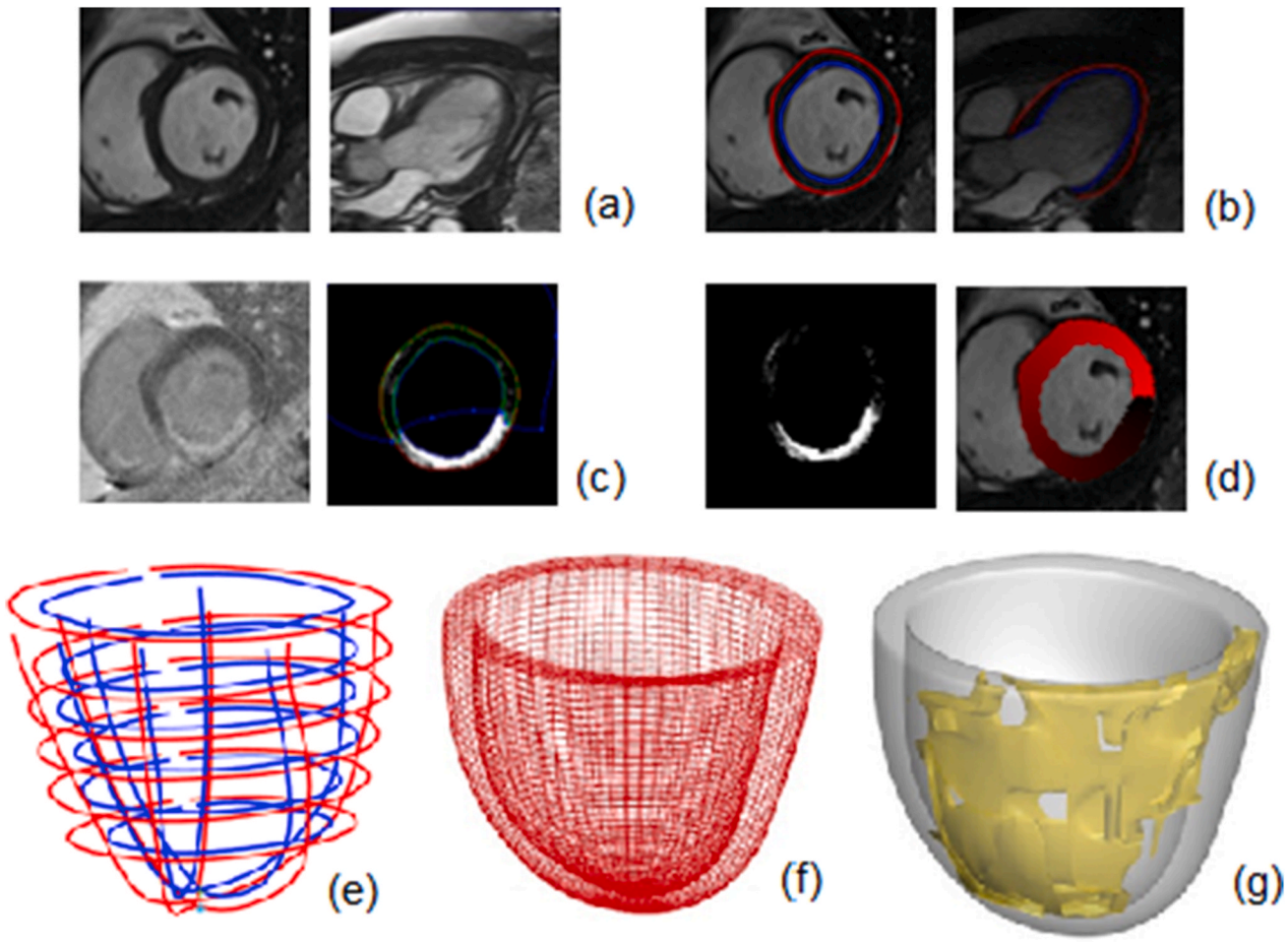


**Fig. 3.** The LV geometry reconstruction and MI region definition from acquired CMR images: (a) cine MRI, (b) segmentation, (c) LGE images and 2D MI contouring, (d) MI 2D mapping, (e) guide point generation, (f) reconstructed LV mesh, (g) the MI region inside the LV shown in yellow.

bandwidth: 930 Hz/pixel, temporal resolution: 46 ms, and matrix size: 180 × 256 with a voxel size of 1.3 × 1.3 × 7 $mm^3$. A set of CMR cine images obtained from patient 9 are shown in Fig. 1.

LGE imaging was further performed 10–15 min after intravenous injection of 0.15 mmol/kg of gadoterate meglumine (Gd2+DOTA, Dotarem, Guebert S.A.). Short-axis and long-axis LGE images were acquired using segmented phase-sensitive inversion recovery in the same planes of cine images. Typical LGE image parameters were flip angle: 25°, TE: 3.36 ms, bandwidth: 130 Hz/pixel, echo spacing: 8.7 ms, trigger pulse: 2, and matrix size: 192 × 256 with a voxel size of 1.8 × 1.3 × 8 $mm^3$. The detailed CMR protocols have been previously reported in Ref. [12].

LV structure and function analyses were carried out as per international recommendation [44]. The basal LV short axial slice was defined as one with >50% of the endocardial border being myocardium. End-diastole was chosen as the cardiac cycle time point with the largest blood-pool volume, and end-systole with the smallest [44]. Analyses were performed on Siemens Syngo VE32D workstation with Argus software (Siemens Healthcare, Erlangen, Germany). Infarction was defined by the presence of late gadolinium myocardial enhancement revealed in orthogonal planes including phase swap acquisitions if required to rule out artefact. The myocardial mass of LGE (grams) was assessed utilizing the five standard deviations method. Microvascular obstruction was identified as a central hypointense core within an area of LGE and defined as present/absent, and quantified as mass (grams) and % LV mass. The patients' characteristics are listed in Table 1.

Changes in the LVEDV have been used to characterize the degree of heart G&R. For example, a criterion of ±12% volume change post-MI has been defined as a clinical measure of G&R [11]. Here we adopt this reference classification using a normalized $LVEDV/LVEDV_0$, where $LVEDV_0$ is the baseline volume at acute-MI state (4–12 h after reperfusion), and categorise the patients into three groups at 7 months post-MI: the Dilation (enlarge ≥ 12%, adverse G&R), No-Change (change < 12%) and Shrinkage (reduction ≥ 12%, reverse G&R) groups.

### 2.2. LV geometry reconstruction and MI delineation

Short-axis and long-axis cine images at end-diastole were selected for the LV geometry reconstruction from each scan. An in-house MATLAB code was developed for image segmentation, template geometry fitting, hexahedral mesh generation, myofibre generation and result visualization. MATLAB was also used to delineate MI in short-axis LGE images and map scarred regions into reconstructed LV geometries. Ventricular geometry reconstruction based on in vivo CMR images and motion corrections were the same as our previous studies [18,20], as illustrated in Fig. 3. Specifically, we.

1. Manually segment LV wall boundaries in cine images from 6 to 7 short-axis planes from base to apex and in 3 orthogonal long-axis images (LVOT, HLA, VLA), as shown in Fig. 1;
2. Correct motion artefacts by aligning the LV wall boundaries in the short-axis cine images to the boundaries in the long-axis cine images (LVOT, HLA, VLA), similar to Ref. [18];

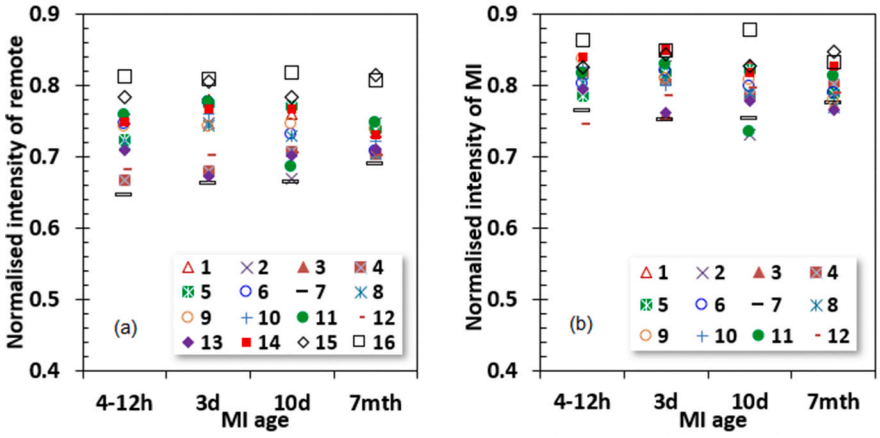


**Fig. 4.** The used intensity thresholds for segmentation of remote and MI zones in terms of MI age.

3. Determine the mass centre of the most basal plane from the delineated LV wall boundaries, and manually define the LV apex from the long-axis images. Then the longitudinal axis is defined by connecting the mass centre of the LV cavity in the basal plane to the LV apex;
4. Locate the MV annular ring position from the LVOT image, then the most basal short-axis images from different scan times are moved along the long-axis by assuming the distances to the MV annular ring are identical for all scans from the same patient;
5. Fit the segmented LV boundaries to a template LV mesh [21,34], in which the mass centre of the ventricular wall in the most basal plane is the original point, with zero degrees lying in the horizontal direction shown in Fig. 2 and moving from the septum segment towards the anterior segment then the inferior wall. The prolate spheroidal coordinate system is described by $(u, v, w)$ where $u$, $v$ and $w$ represent azimuthal, meridional and thickness coordinates, respectively. Specifically, for any point with Cartesian coordinate $(x, y, z)$, the corresponding spheroidal coordinates $(u, v, w)$ are

$$\begin{cases} x &= \alpha \sinh(w) \cos(u) \cos(v) \\ y &= \alpha \sinh(w) \cos(u) \sin(v) \\ z &= \alpha \cosh(w) \sin(u), \end{cases} \tag{1}$$

in which $\alpha$ is a scaling factor, $u \in [-\pi/2, \quad \pi/2)$, $v \in [0, \quad 2\pi)$, and $w \in (0, \quad +\infty)$. By aligning the most-basal plane to the $z = 0$ plane, we have $u = 0$ at the basal plane and $u = -\pi/2$ at the apex. We then consider values of $w$ of the segmented boundary points on the LV endocardial and epicardial contours are best fitted with respect to $u$ and $v$ using the cubic B-spline functional, that is

$$f_{\text{endo}} = \frac{1}{N} \sum_{n=1}^{N} \gamma_n [w_{\text{endo}}(u_n, v_n) - w_n]^2, \tag{2}$$

in which $N$ is the total number of known segmented points on the surface, $u_n$, $v_n$ and $w_n$ are calculated from (1), $\gamma_n$ is the interpolation coefficient from the cubic B-spline functional, and $f_{\text{endo}}$ is the error function to be minimized. Geometric regularization is further imposed to avoid large curvature on the fitted surface. Please refer to Ref. [34] for more details on this LV geometry fitting.

6. Define the septal segments, and match the RV-LV insertion points in the basal plane across different geometries of the same patient in such way that the inferior RV insertion points have the same coordinates $(u, v)$, and the same number of elements along the circumferential direction is assigned for the septum segments, as shown in Fig. 2;
7. Generate rule-based myofibre structures as previously described in Ref. [52]. The mean fibre angle (measured from the circumferential direction) varies linearly from $-60^\circ$ at epicardium to $60^\circ$ at endocardium, and the mean sheet angle is $-45^\circ$ at epicardium and $45^\circ$ at endocardium measured from the radial direction in each element.

Note that steps 3 and 4 align the LV geometries longitudinally at different scan times from each patient, then steps 5 and 6 align the LV geometries circumferentially for the same patient. Hence, all four LV geometries from each patient are spatially co-registered.

In order to compare the G&R between MI and remote zones, we further delineate the MI regions from corresponding short-axis LGE images at 4–12 h (baseline), 3 days, 10 days and 7 months after reperfusion, and then map them into the reconstructed LV geometry, as shown in Fig. 3. Specifically, we.

1. Identify LGE images from the most basal short-axis plane to the apex, and export corresponding short-axis cine images at the same cardiac phase (normally mid-diastole);
2. Manually segment LV boundaries for both short-axis cine and LGE images at mid-diastole, similar to LV wall segmentation in cine images;
3. Define the remote, MI regions and MVOs from LGE images, then assign intensity from 0 to 1 to all regions such that 0 indicates the functional myocardium, and 1 is the most infarct region, including MVOs. Here the k-means algorithm from MATLAB is adopted to determine a threshold for MI size determination, which is fast and simple to implement, and can automatically distinguish healthy and infarct myocardium [25,35];
4. Map LGE intensities to short-axis cine images at mid-diastole by assuming the LV wall boundary is unchanged from both LGE and cine short-axis images because they were acquired at the same cardiac phase;
5. Apply a cubic B-spline deformable registration method to deform the LV wall from mid-diastole to early-diastole [19], then transfer the map of regional intensity from mid-diastole to end-diastole;
6. Interpolate mapped LGE intensities from short-axis cine images to the reconstructed 3D LV geometry. Linear interpolation is used for regions between the two short-axis slices. Special treatment is needed in the region between the most apical short-axis image and the apex. If the apex is infarcted as evidenced in the long-axis LGE images, then the intensity at the apex is 1, otherwise 0. Intensities in-between are linearly interpolated.

Note that in order to classify MI regions in the LGE images, we first normalized pixel intensity in the range of $[0, 1]$, 0 is for functional myocardium, and 1 is for the most infarcted region, MVO included. The intensity threshold determined from the k-means algorithm with 2 clusters is around $0.65 - 0.83$ for the remote region and $0.75 - 0.88$ for

the MI region, which varies because of different imaging characteristics of different scans and different subjects. The threshold values for delineating MI and remote regions are summarized in Fig. 4.

Once the LV is reconstructed from different scans for each patient, the cavity volume, ventricular wall volume and MI size can be readily calculated.

### 2.3. Estimation of the growth tensor

The most commonly used continuum mechanics approach for modelling G&R is known as the volumetric growth [1,41,48]. This is based on a multiplicative decomposition of the deformation gradient, $\mathbf{F} = \mathbf{F}^e\,\mathbf{F}^g$, where $\mathbf{F}^g$ is the (pure) growth tensor, and $\mathbf{F}^e$ accounts for the elastic response of myocardium under mechanical loadings. The key to modelling the G&R process is the determination of $\mathbf{F}^g$ and its evolution with time. Different forms of the growth tensor $\mathbf{F}^g$ have been hypothesised in the literature, from isotropic [28], transversely isotropic [48], to general anisotropic forms [1], whose evolution may be driven by stress or strain, or both [23].

In this study, a template LV FE mesh with 8-node bricks is wrapped to the segmented LV boundaries, with the same element connectivity and numbering for each patient. This allows us to align all the LV geometries from different scans. It is then reasonable to assume the m$^{\text{th}}$ element of the four scans are co-registered, that is

$$E_0^m(n_1,n_2,\ldots,n_8)\rightarrow E_{3\text{d}}^m(n_1,n_2,\ldots,n_8)\rightarrow E_{10\text{d}}^m(n_1,n_2,\ldots,n_8)\rightarrow E_{7\text{mth}}^m(n_1,n_2,\ldots,n_8), \tag{3}$$

where $E_0^m$ , $E_{3\text{d}}^m$ , $E_{10\text{d}}^m$ and $E_{7\text{mth}}$ are the m$^{\text{th}}$ element at the respective instants, e.g. 4–12 h, 3-day, 10-day and 7-month after reperfusion, and $n_1, n_2, \ldots, n_8$ are the eight nodes of the element. A shape change descriptor of these elements is provided by the deformation gradient tensor:

$$\mathbf{F} = \frac{\partial \mathbf{x}}{\partial \mathbf{X}_0} = \mathbf{F}^e\,\mathbf{F}^g, \tag{4}$$

where $\mathbf{x}$ is the position vector of the current configuration, $\mathbf{X}_0$ is the position vector at a stress-free reference configuration. $\mathbf{F}^e$ is the elastic deformation tensor due to loading, and $\mathbf{F}^g$ is the growth tensor. However, the stress-free reference configuration is unknown, so instead, we use the loaded acute state (baseline) $\mathbf{x}_b$ as the reference configuration, which is not stress-free, and track the growth information between the two scans,

$$\mathbf{G} = \frac{\partial \mathbf{x}}{\partial \mathbf{x}_b}. \tag{5}$$

We now explain the relationship between $\mathbf{G}$ and $\mathbf{F}^g$. Let $\mathbf{X}_0$ and $\mathbf{X}_{0b}$ indicate the unloaded and stress-free configurations between the current and baseline scans, respectively, then the change between the two unloaded configurations, $\mathbf{X}_0$ and $\mathbf{X}_{0b}$, can only be due to the material growth,

$$\mathbf{F}^g = \frac{\partial \mathbf{X}_0}{\partial \mathbf{X}_{0b}}. \tag{6}$$

(5) can be rewritten as

$$\mathbf{G} = \frac{\partial \mathbf{x}}{\partial \mathbf{X}_0}\frac{\partial \mathbf{X}_0}{\partial \mathbf{X}_{0b}}\frac{\partial \mathbf{X}_{0b}}{\partial \mathbf{x}_b} = \mathbf{F}^e\mathbf{F}^g\left(\mathbf{F}_b^e\right)^{-1}, \tag{7}$$

where $\mathbf{F}_b^e$ is the end-diastole elastic deformation at the baseline related to $\mathbf{X}_{0b}$, and $\mathbf{F}^e$ is the elastic deformation of the current scan related to $\mathbf{X}_0$. In other words, $\mathbf{G}$ contains not only the growth tensor, but also the elastic deformations due to loading at the baseline and the current scans. Note $\mathbf{G}$ is equal to $\mathbf{F}^g$ only at the two special cases:

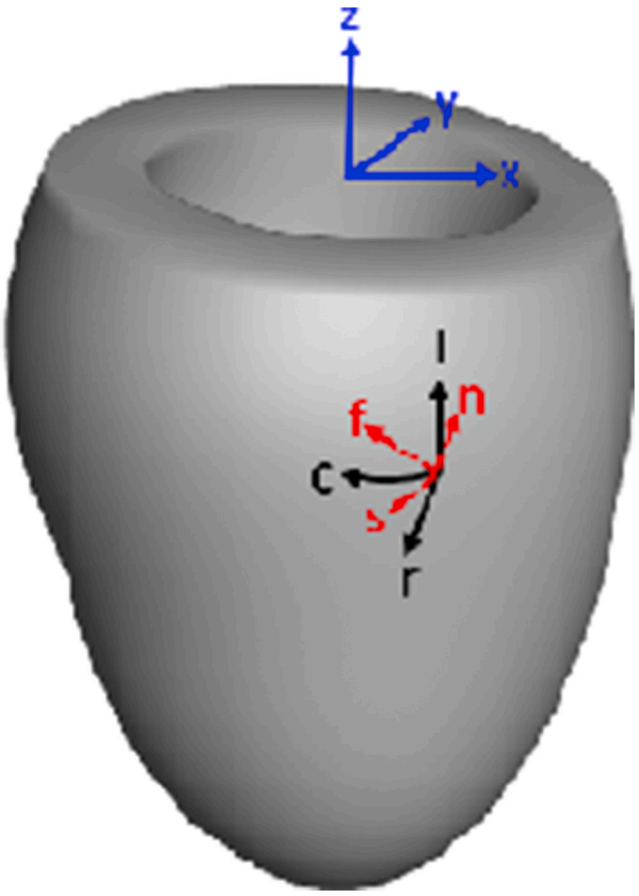


**Fig. 5.** Schematic illustration of the LV model and the circumferential-radial-longitudinal coordinate and the fibre-sheet-normal coordinate systems, $(\mathbf{x}-\mathbf{y}-\mathbf{z})$ is the global Cartesian system, $(\mathbf{c}-\mathbf{r}-\mathbf{l})$ is the cosine matrix of the circumferential-radial-longitudinal directions with respect to the $(\mathbf{x}-\mathbf{y}-\mathbf{z})$, and $(\mathbf{f}-\mathbf{s}-\mathbf{n})$ is the cosine matrix of the myofibre-sheet-normal directions related to $(\mathbf{c}-\mathbf{r}-\mathbf{l})$.

1) the elastic deformations at the two scan times are similar and no growth, i.e.

$$\mathbf{F}^e\left(\mathbf{F}_0^e\right)^{-1} \approx \mathbf{I},\ \mathbf{F}^g = \mathbf{I}, \tag{8}$$

then

$$\mathbf{G} = \mathbf{F}^e\left(\mathbf{F}_0^e\right)^{-1} = \mathbf{I} = \mathbf{F}^g, \tag{9}$$

2) if $\mathbf{F}^g$, $\mathbf{F}_0^e$, and $\mathbf{F}^e$ are all diagonal, i.e. growth and deformations are in the principle directions, then $\mathbf{F}^g$ and $\mathbf{F}^e$ commute, and

$$\mathbf{G} = \mathbf{F}^g\mathbf{F}^e\,\mathbf{F}_0^{e-1} = \mathbf{F}^g. \tag{10}$$

In general, these assumptions do not hold, hence $\mathbf{G}$ is only an approximation of $\mathbf{F}^g$. From the reconstructed FE models of the LV, we can compute all the components of $\mathbf{G}$. Hence, $\mathbf{G}$ can be used as a convenient surrogate for $\mathbf{F}^g$, or the apparent growth tensor. Indeed, since the unloaded stress-free configurations are difficult to be measured even from animal hearts, most of the current growth theories are developed based on these approximations [26,39,49]. Extracting $\mathbf{F}^g$ is theoretically possible with additional measurements (loading and residual stress). Since these measurements are not available, we do not pursue it in this paper. In the following, we discuss features of $\mathbf{G}$ as an estimate of "growth tensor".

In the circumferential-radial-longitudinal system, we have

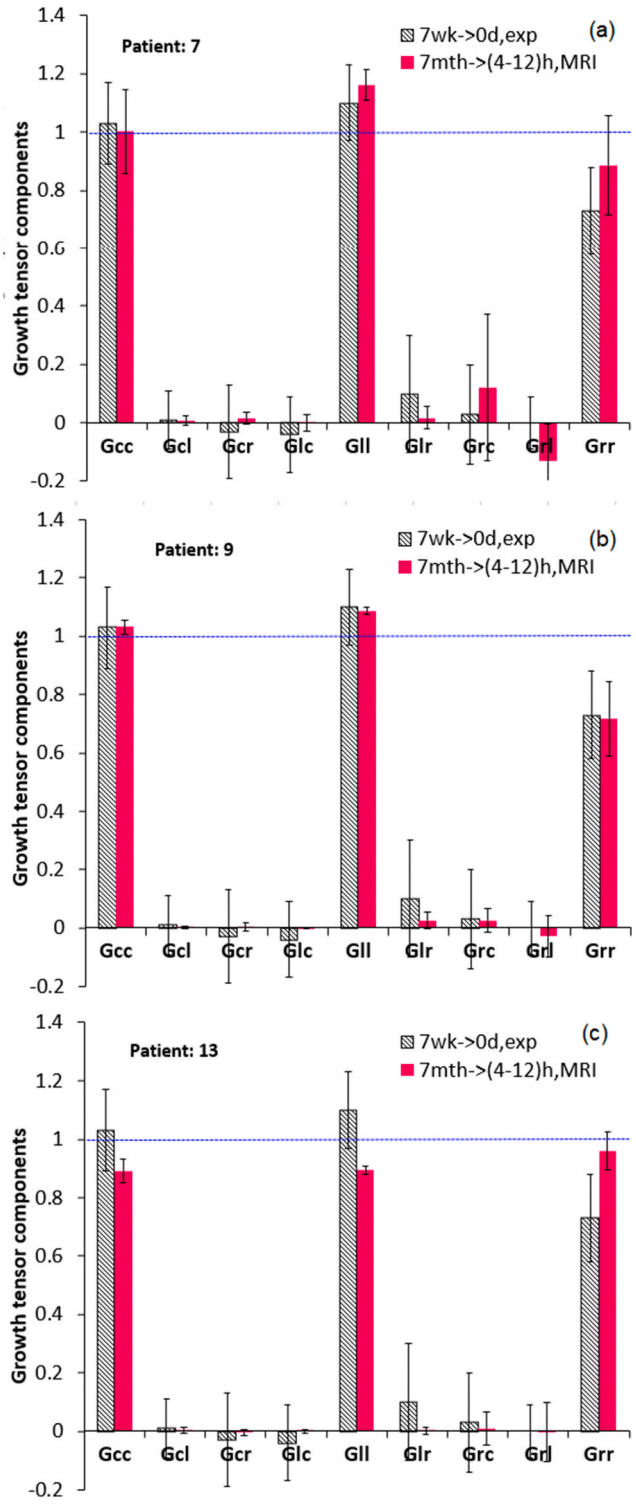


**Fig. 6.** Comparison of measured and estimated growth tensor components in the MI zone, the measurements are taken from Tsamis et al. [49], and the estimations are from patients (a) 7 (Dilation), (b) 9 (No-Change), f and (c) 13 (Shrinkage) in our study.

$$\mathbf{G}_{\mathrm{crl}} = \mathbf{Q}_{\mathrm{crl}}\mathbf{G}\mathbf{Q}_{\mathrm{crl}}^{\mathrm{T}}, \tag{11}$$

where $\mathbf{Q}_{\mathrm{crl}}$ is the cosine matrix of the circumferential-transmural-longitudinal directions as shown in Fig. 5. Similarly, in the myofibre-sheet-normal system, we have

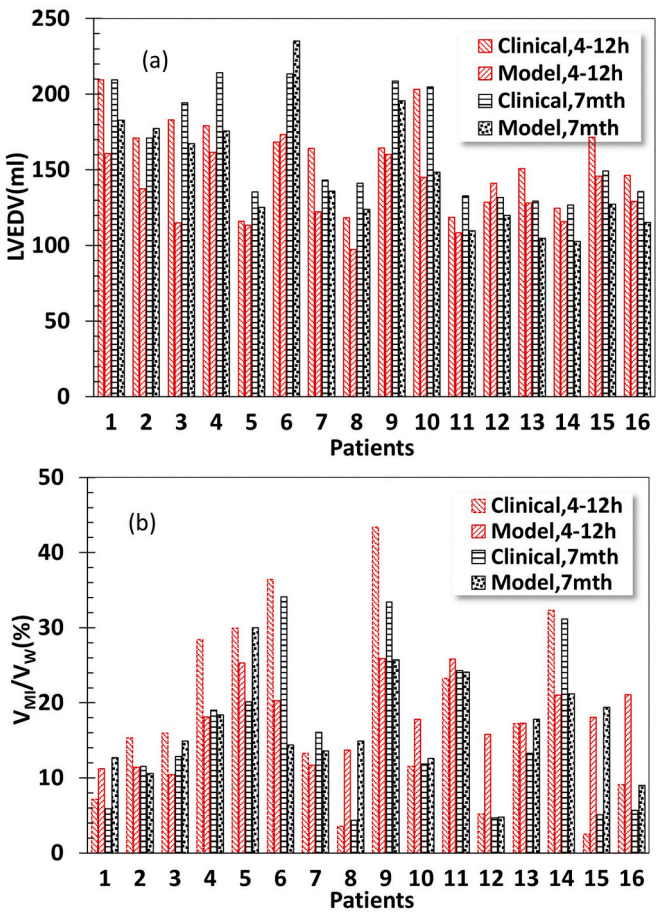


**Fig. 7.** The LVEDV (top) and MI-LV wall (bottom) volume ratios for 16 patients at 4–12 h and 7 months post-MI. These model results are compared with those obtained clinically.

$$\mathbf{G}_{\mathrm{fsn}} = \mathbf{Q}_{\mathrm{fsn}}\mathbf{G}\mathbf{Q}_{\mathrm{fsn}}^{\mathrm{T}}, \tag{12}$$

where $\mathbf{Q}_{\mathrm{fsn}}$ is the cosine matrix of the myofibre-sheet-normal directions, as shown in Fig. 5. In the following, both systems are used to help with the physical interpretation of growth tensor inside the LV.

To test that our **G** has the characteristics of the true growth, we first present the **G** components in the ($\mathbf{c}-\mathbf{r}-\mathbf{l}$) system so as to compare with published experimental results based on beads insertion in sheep LV. Fig. 6 shows the comparison between the LV-averaged growth tensor components at the MI region in patients 7 (Dilation), 9 (No-Change), 13 (Shrinkage) at 7-month post-reperfusion against the measured in vivo growth tensors at mid-myocardium from a sheep myocardial infarction experiment at 7 weeks post-MI [49]. Here, our growth tensor is calculated at 10 days post-MI, to be consistent with the experimental study in which the **G** was calculated at 1-week post-MI.

Our estimated growth components $G_{\mathrm{cc}}$ (along the circumferential direction), $G_{\mathrm{ll}}$ (along the longitudinal direction), $G_{\mathrm{rr}}$ (along the radial direction) exhibit good agreement with the in vivo measurements [49], particularly for patient 9, suggesting the measured heart is more likely to have no significant LVEDV change. Most significantly, both the growth tensors from our study and the in vivo sheep experiment are strongly diagonal dominant. Likewise, **G** is diagonally dominant in the fibre-sheet-normal ($\mathbf{f}-\mathbf{s}-\mathbf{n}$) system (not shown). This provides the rationale for assuming **G** to be diagonal. Hence, in the following, we only present the diagonal components of the growth tensor.

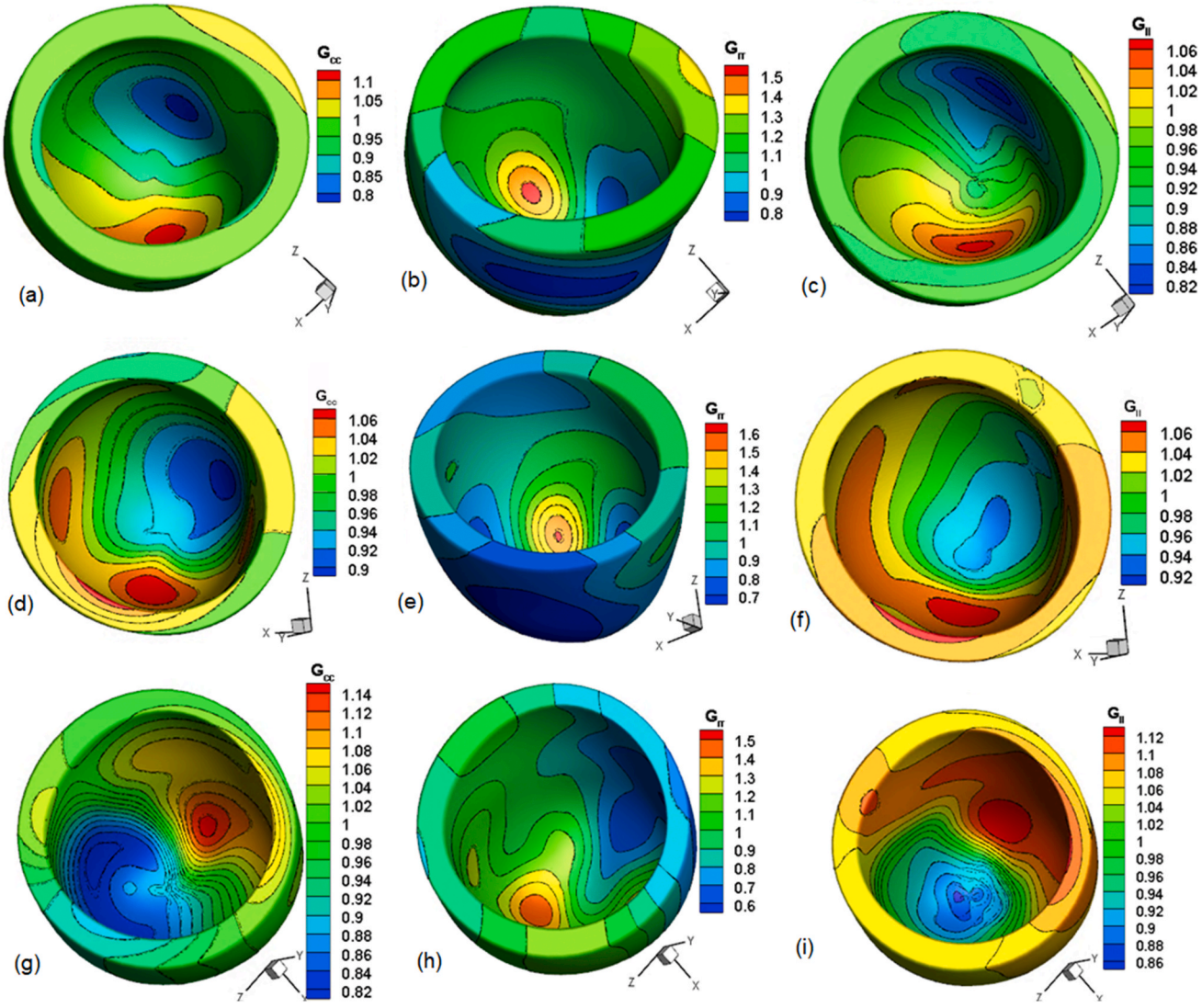


**Fig. 8.** The contours of $G_{cc}$, $G_{rr}$, $G_{ll}$ at 3-day, 10-day and 7-month post-MI for patient 9. The solid lines are for default mesh and dashed lines are for the refined mesh, (a)–(c) for 3-day, (d)–(f) for 7-day, (g)–(i) for 7-month.

### 2.4. Statistics

Parameters of interest for each group are reported as mean and standard deviation, including LVEF, MVO extent, ventricular wall volume and its normalization. Time-dependent growth tensors are summarized at both the functional and the MI regions in **f**− **s**− **n** and **c**− **r**− **l** systems. The difference between the Dilation and Shrinkage groups are determined using the Microsoft Excel two-sample *t*-test. A statistically significant difference is taken at the level $p < 0.05$. Because there are only 2 subjects in the No-Change group, statistics for this group was not performed.

## 3. Validations

Validation 1: the LVEDV and the MI volume ratio ($V_{MI}/V_w$) from our reconstructions are compared with the measurements obtained by K.M. at 4–12 h and 7 months post-MI, as shown in Fig. 7. In general, good agreement of the LVEDV volume ratio is observed between clinical assessment and values derived from our 3D reconstructions with a mean error (clinical - reconstruction) of +14.43% at 4–12 h and +11.13% at 7 months, respectively. Excellent agreement of the MI volume ratio is also achieved with a mean error (clinical - reconstruction) of +3.27% at

**Table 2**
Average G&R and standard deviation (std) for patient 9 along the circumferential, longitudinal and radial directions at three different times post-MI.

| | Default mesh | | Refined mesh | |
|---|---|---|---|---|
| G&R | Average | Std | Average | Std |
| **3 days** post reperfusion | | | | |
| $G_{cc}$ | 0.9689 | 0.0581 | 0.9687 | 0.0581 |
| $G_{rr}$ | 1.0384 | 0.1473 | 1.0386 | 0.1479 |
| $G_{ll}$ | 0.9471 | 0.0416 | 0.9469 | 0.0415 |
| **10 days** post reperfusion | | | | |
| $G_{cc}$ | 0.9806 | 0.0352 | 0.9805 | 0.0352 |
| $G_{rr}$ | 0.8997 | 0.1627 | 0.8995 | 0.1627 |
| $G_{ll}$ | 1.0055 | 0.0370 | 1.0054 | 0.0371 |
| **7 months** post reperfusion | | | | |
| $G_{cc}$ | 0.9631 | 0.0695 | 0.9619 | 0.0699 |
| $G_{rr}$ | 0.9927 | 0.2020 | 0.9928 | 0.2016 |
| $G_{ll}$ | 1.0192 | 0.0677 | 1.0189 | 0.0683 |

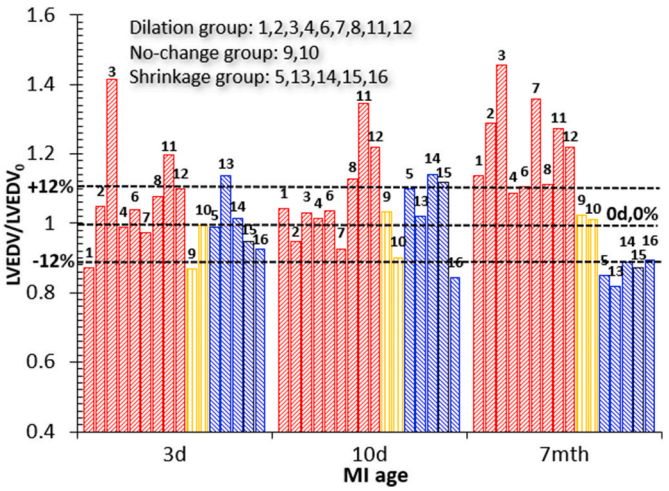


**Fig. 9.** Normalized LVEDV scaled by the baseline value of all 16 patients at 3 days, 10 days and 7 months after reperfusion. The 12% volume change is used to classify the Dilation (red, line up), No-Change (yellow, line flat), and Shrinkage (blue, line down) groups.

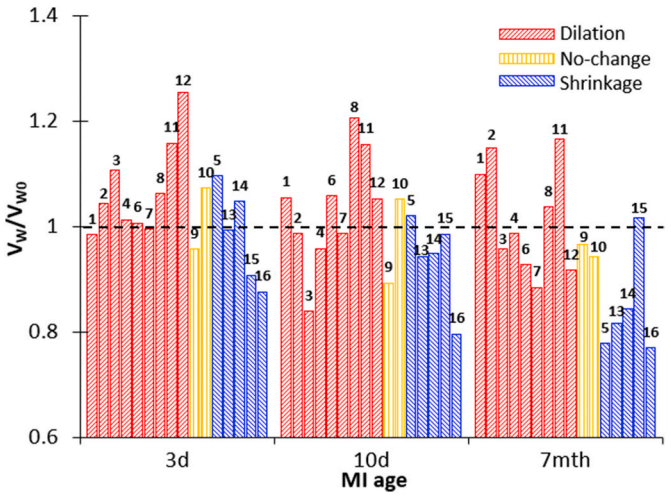


**Fig. 10.** Normalized LV wall volume scaled by the corresponding baseline value.

**Table 3**
Classification of patient groups, compared with group-averaged clinical indices at the baseline (acute) and seven-month follow up.

| Indices | Dilation | No-Change | Shrinkage | Dilation vs Shrinkage ($p$) |
|---|---|---|---|---|
| Patient No. | 1,3,4,6,7,8,11,12 | 9, 10 | 5, 13, 14, 15, 16 | |
| MVO extent (%LV mass) | 4.66±4.55 | 3.58 ±5.06 | 1.81±4.05 | 0.130 |
| LVEF (acute %) | 54.88±13.83 | 55.15 ± 5.16 | 57.72±7.03 | 0.310 |
| LVEF (follow up %) | 56.91±9.45 | 60.5±15.41 | 67.16±6.10 | 0.015 ($p$ <0.05) |
| Myocardial salvage (%LV mass) | 16.77±9.50 | 15.13±8.46 | 23.38±13.21 | 0.181 |
| MI size (acute) (%LV mass) | 21.49±13.63 | 17.38±8.28 | 13.26±11.99 | 0.136 |
| MI size (follow up) (%LV mass) | 17.49±10.65 | 18.06±8.79 | 11.98±11.30 | 0.199 |
| Peak Troponin I (ug/L) (acute) | 7099.4± 5471.9 | 6315.5±1564.8 | 5125.0± 6439.2 | 0.290 |

4–12 h and −4.21% at 7 months after acute MI. Additionally, to assess error in the manual reconstruction, we reconstructed the LV geometry of patient 4 at 4–12 h post-MI five times. The errors in the LVEDV and LV wall volumes, defined as the ratio between their standard deviations and the mean values, respectively, are +0.64% and +1.49% only.

Validation 2: A template mesh with 50 (longitudinal) × 60 (circumferential) × 10(transmural) elements is used for representing the LV geometry, the same mesh has been used for FE modelling of LV dynamics [33]. To check whether this mesh is adequate for estimating $\mathbf{F}^g$, the mesh of patient 9 is refined with 60 (longitudinal) × 84 (circumferential) × 14 (transmural) elements. The contours of $G_{cc}$, $G_{rr}$ and $G_{ll}$ at 3 days, 10 days and 7 months post-MI are shown in Fig. 8, and their average values are further summarized in Table 2. The results are almost identical for the two different meshes. Therefore, the default mesh size (50 × 60 × 10) is used in the following analysis.

Validation 3: Direct validation of the growth tensors is challenging because invasive measurements are needed to measure $\mathbf{F}^g$. Hence, we seek indirection validation by comparing the average $\mathbf{F}^g$ of patients 7, 9 and 13 in MI regions at 7 months post-MI with published experimental data based on sewing beads in sheep LV walls [49]. Fig. 6 shows that the growth tensors of all three patients agree well with the measurements [49]. This good agreement suggests that estimation of $\mathbf{F}^g$ from in vivo CMR images is feasible, although quantitative validation of $\mathbf{F}^g$ (e.g. based on parallel animal experiments) would be desirable in future.

**Table 4**
Group averaged LV wall volume, scaled by its value at the baseline, $V_w/V_{w0}$, for the patient groups, at 3 days, 10 days, and 7 months follow-up post-MI.

| | Dilation | No-Change | Shrinkage | Dilation vs Shrinkage ($p$) |
|---|---|---|---|---|
| $V_w/V_{w0}$ (3 days) | 1.06±0.08 | 1.01 ±0.08 | 0.98±0.09 | 0.073 |
| $V_w/V_{w0}$ (10 days) | 1.06±0.15 | 0.97 ±0.11 | 0.94±0.09 | 0.035 ($p$ <0.05) |
| $V_w/V_{w0}$ (7 months) | 1.05±0.13 | 0.95 ±0.02 | 0.85±0.10 | 0.004 ($p$ <0.05) |

## 4. Results

Fig. 9 shows the normalized LVEDV changes (LVEDV/LVEDV$_0$) at 3 days, 10 days and 7 months after reperfusion. According to the criterion of a ±12% LVEDV change at 7-months post-MI [11], out of 16 patients, nine (ID: 1, 2, 3, 4, 6, 7, 8, 11, 12) (56.25%) are in the Dilation group; two (ID: 9, 10) (12.5%) are in the No-Change group, and five (ID: 5, 13, 14, 15, 16) are in the Shrinkage group. The averaged clinical indices at baseline and 7-month follow up for the three groups are listed in Table 3. By definition, the Dilation group reflects adverse LV remodelling, and the Shrinkage group reflects favourable or reverse remodelling. However, with the exception of LVEF at 7-month follow-up, none of the clinical indices is associated with between-group differences in size in part due to the limited sample size and lack of power.

Fig. 10 shows the normalized LV wall volume of all the patients, defined as V$_w$/V$w$0 where V$_{w0}$ is the baseline LV wall volume. The group-averaged values are shown in Table 4. No statistically important changes are seen in the three groups at 3 days post-MI. However, at 10- days and 7 months after myocardial reperfusion, the difference of V$_w$/V$_{w0}$

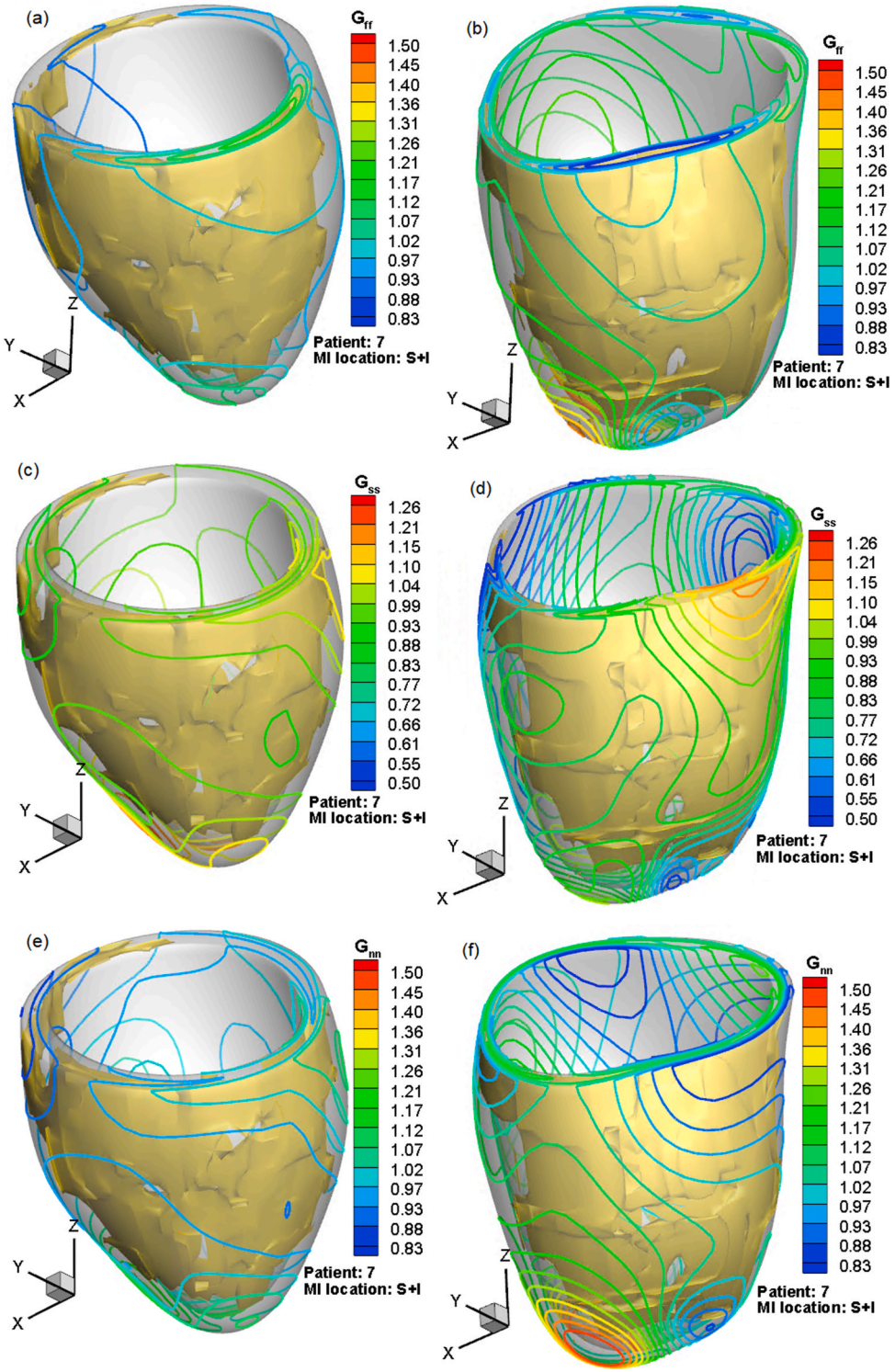


**Fig. 11.** LV geometry with MI region and contours of ($G_{ff}$, $G_{ss}$, and $G_{nn}$) for patient 7 in the Dilation group, the yellow-coloured volume is the MI region. Left panel: short-term (10-day post-MI), right panel: long-term (7-month post-MI). Notice that a large portion of the LV is occupied by the MI.

between the Dilation and Shrinkage groups is statistically significant ($p < 0.05$), with the wall volume reduction most pronounced in the Shrinkage group.

We now explore the myocardium regional changes based on the apparent growth tensor **G**. The three dimensional LV geometry along with MI, as well as the distribution of the **G** components in the (**f** – **s** – **n**) system for patients 7, 9, and 13 are shown in Figs. 11–13 at different time-points. From Figs. 11–13, we note that the LV shape can be quite different over the 7-month period after reperfusion. The most significant LV shape change is seen in the Dilation case, in which the apex is rounder and the shape is more irregular. No significant shape change is seen in patient 9. In the Shrinkage case, the wall becomes thicker and the LV is smaller at 7 months post-MI. However, the shape change is less obvious than the Dilation group. These features are consistent with the LV-averaged growth tensor components in Fig. 6.

Fig. 14 shows region-averaged **G** components for the MI and remote

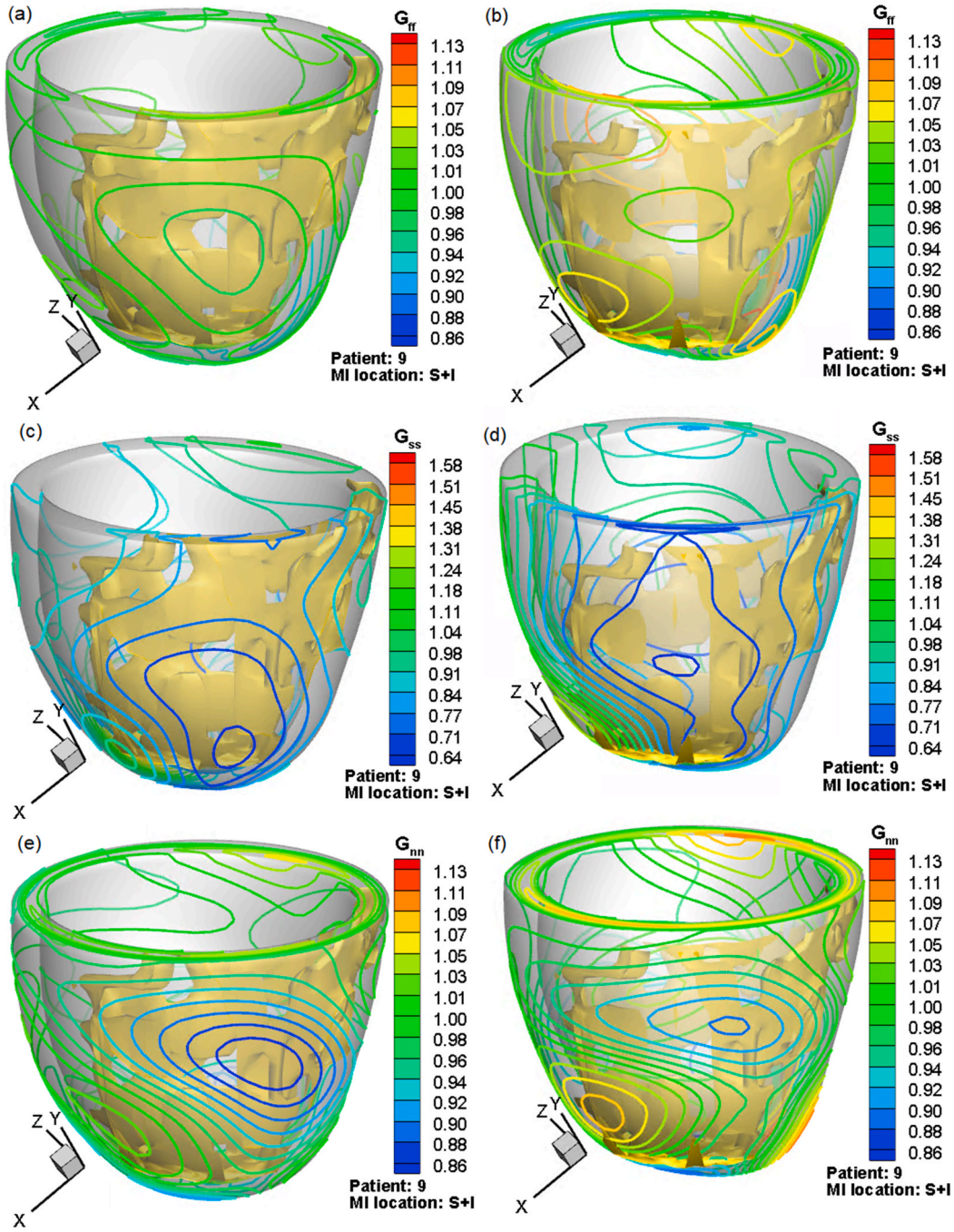


**Fig. 12.** LV geometry with MI region and contours of ($G_{ff}$, $G_{ss}$, and $G_{nn}$) for patient 9 in the No-Change group, the yellow-coloured volume is the MI region. Left panel: short-term (10-day post-MI), right panel: long-term (7-month post-MI).

regions for all three groups, in both the (**c** – **r** – **l**) and (**f** – **s** – **n**) systems. It is clear that despite the difference in magnitudes, the changes of the components are similar either in the (**c** – **r** – **l**) or the (**f** – **s** – **n**) systems. In particular, we note that $G_{ff}$, $G_{ss}$, and $G_{nn}$ follow a similar trend as $G_{cc}$, $G_{rr}$ and $G_{ll}$, respectively. Hence, we focus on discussing the changes of $G_{ff}$, $G_{ss}$, and $G_{nn}$ only. For the Dilation group (Fig. 14(a,b)), all components are above 1 at 10 days after reperfusion for both the remote and MI regions, suggesting the LV experiences an initial dilation and swelling in the short term, possibly due to reperfusion caused oedema. After 7-month G&R, $G_{ff}$ and $G_{nn}$ both increase to beyond 1, but $G_{ss}$ drops rapidly. This suggests that the LV wall becomes much thinner, but elongates in the fibre and sheet-normal directions. The increase of $G_{ff}$ and $G_{nn}$ is associated with the stretch of myocytes. The difference in the growth between the MI and remote regions is small.

Significantly, Fig. 14(c, d) shows an interesting growth pattern for the No-Change group, despite little change in LVEDV. Within the MI region, there are increases in $G_{ff}$ and $G_{nn}$, much more obvious than in the Dilation group, together with a drop in $G_{ss}$ (wall-thinning). However, in the remote region, very little changes are seen in $G_{ff}$ and $G_{nn}$, though $G_{ss}$ decreases with time. The fact that two major G&R components in the remote region don't follow the local change in the MI region is perhaps the reason for the unchanged LVEDV in this group.

The average G&R components in the Shrinkage group can be found in Fig. 14(e, f). These are quite different from the Dilation group (Fig. 14 (a, b)). At 10 days post-MI, the only $G_{ss}$ is slightly over 1 in the remote region. All other components are below 1, and decrease further at 7

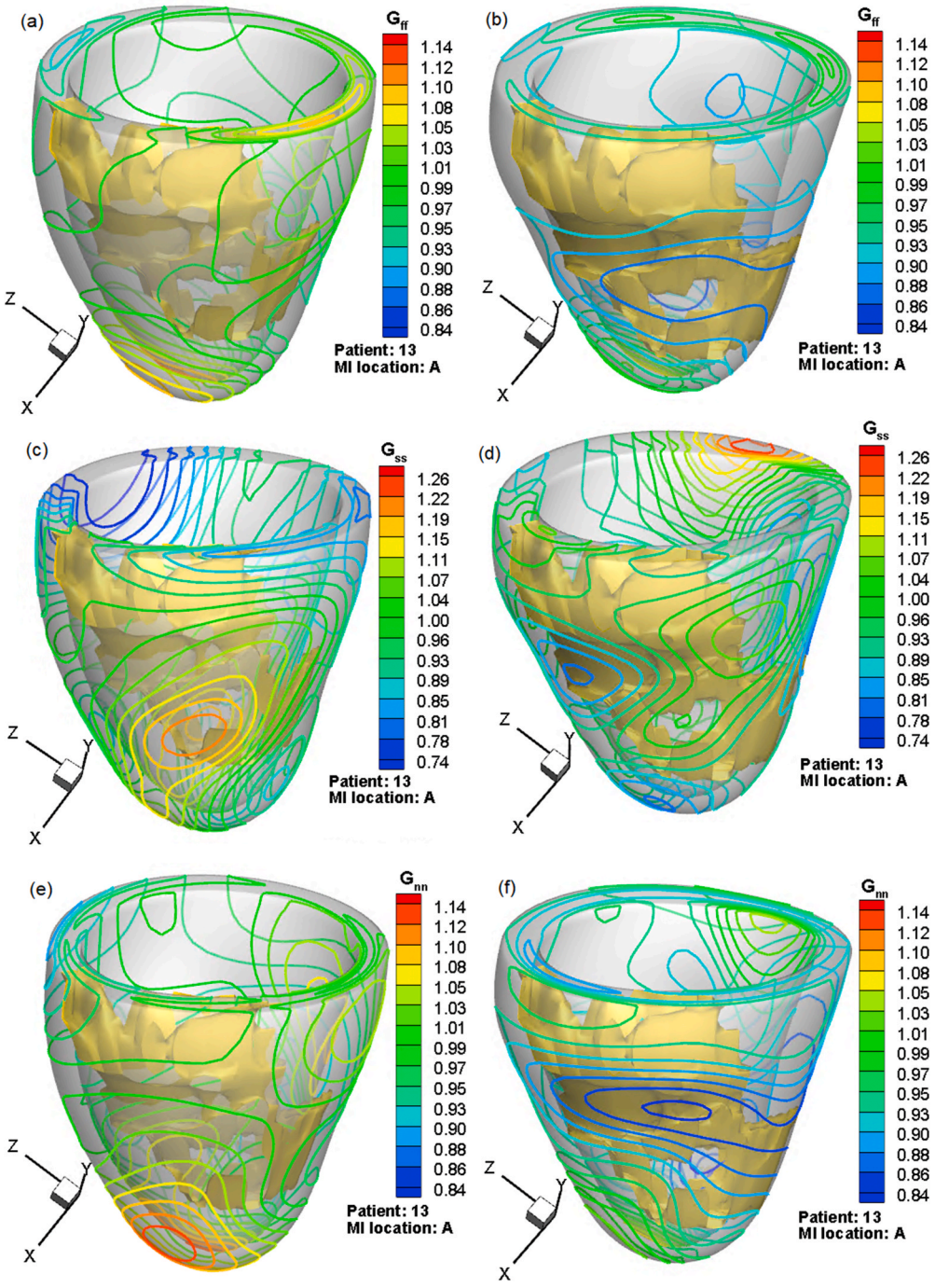


**Fig. 13.** LV geometry with MI region and contours of ($G_{ff}$, $G_{ss}$, and $G_{nn}$) for patient 13 in the Shrinkage group, the yellow-coloured volume is the MI region. Left panel: short-term (10-day post-MI), right panel: long-term (7-month post-MI).

months. Contrary to the other two groups, $G_{ss}$ decrease slows down after 10 days. This suggests the wall-thinning stops sooner in this group. On the other hand, $G_{ff}$ and $G_{nn}$ continue to decrease in the longer term, and both the MI and remote regions follow similar trends.

More insight into the growth tensor can be provided by its invariants, which are independent of the local coordinates. Fig. 15 shows the group and region-averaged invariants $I_1$, $I_2$ and $I_3$ of the growth tensor $\mathbf{G}$, in which $I_1 = \mathrm{tr}(\mathbf{G}^{\mathrm{T}}\,\mathbf{G})$ $I_2 = [(\mathrm{tr}\ \mathbf{G}^{\mathrm{T}})^2 - \mathrm{tr}\ \mathbf{G}^2]/2$, and $I_3 = \det(\mathbf{G})$. $I_1$ is the sum of the squared G&R components in principal directions, i.e. $I_1 \approx G_{ff}^2 + G_{ss}^2 + G_{nn}^2$. $I_1 < (>)3$ suggests there is shrinkage/dilation in one, two or all directions. The physical meaning of $I_2$ is harder to define, but it is loosely related to the shape or area change if its value deviates from $I_2 = 3$ (the baseline value). $I_3$ indicates the wall volume change, $I_3 > 1(< 1)$ means a wall mass decrease/increase, which is not the same as the LVEDV change.

It is clear that in the Dilation group, both $I_1$ and $I_2 > 3$, though $I_1$ decreases back to the baseline value at 7 months post-MI, presumably because the increase in $G_{ff}$ and $G_{nn}$ outweigh the reduction in $G_{ss}$ at both the MI and remote regions (Fig. 14(a, b)). In the Dilation group, $I_3$ is always above 1, which is more obvious in the long-term growth, indicating the total wall mass increases as the LVEDV expands, despite the wall thinning. In the Shrinkage group, all invariants reduce, the wall becomes thinner and total wall mass also drops (compared to the baseline). We note that in both the Dilation and Shrinkage groups, the

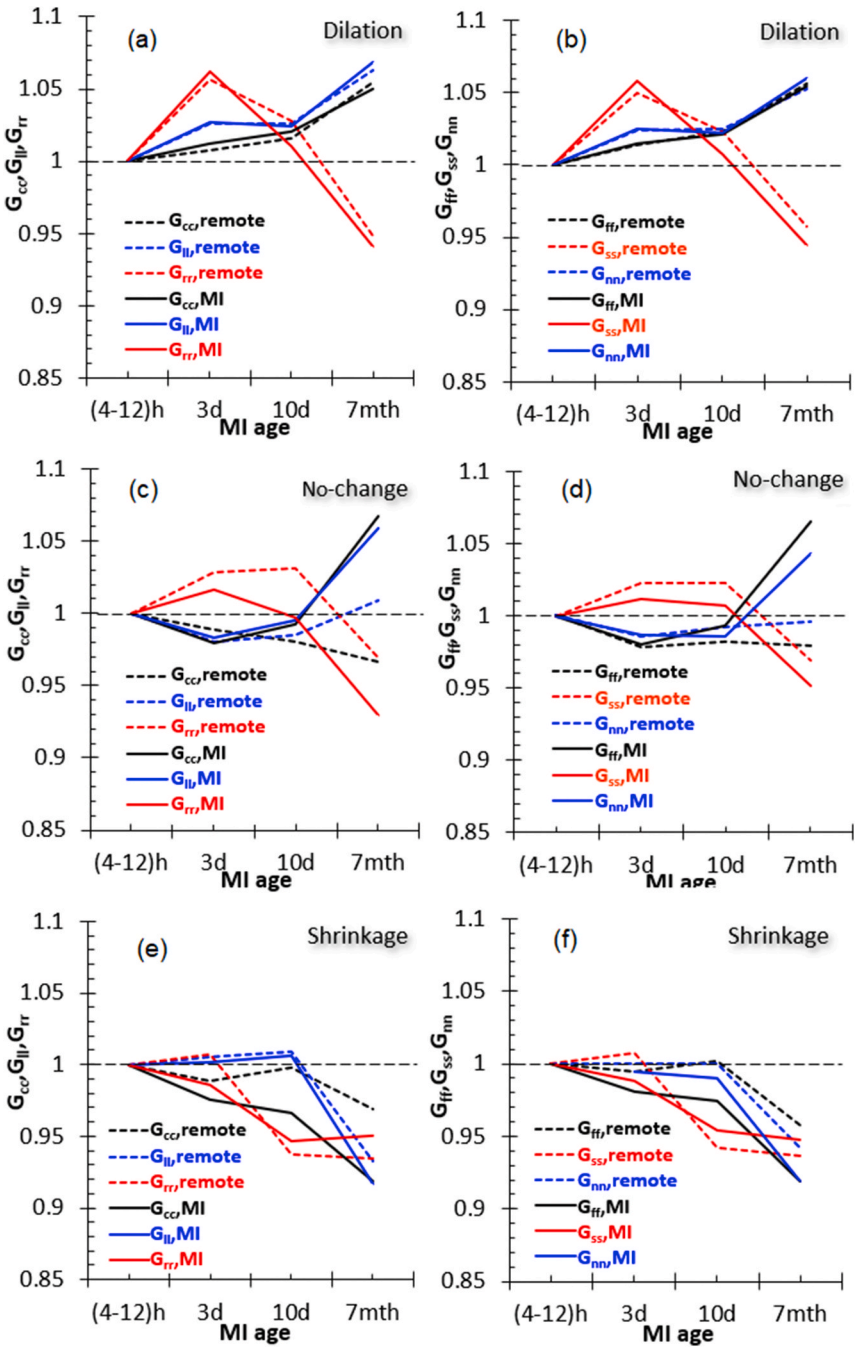


**Fig. 14.** Group averaged $G_{cc}$, $G_{rr}$, $G_{ll}$ (left) and $G_{ff}$, $G_{ss}$, $G_{nn}$ (the right panel) at 10-day and 7-month post-MI for the Dilation, No-Change and Shrinkage groups, respectively. The solid lines are for the MI region and dashed lines are for the remote region, error bars are not shown, standard deviations of the bars have been included in Table 5.

trends of the MI and remote regions are similar. In the No-Change group, however, the interpretation is different. In the remote region, $I_1$ and $I_3$ decrease first but then increase back to the baseline values. In the MI region, $I_1$ remains more or less unchanged after 10 days and $I_3$ continues to decrease. This means that the wall mass loss is localized around the MI region. $I_2$ drops below 3 in both the MI and remote regions, similar to that of the Shrinkage group.

The tensor components of the averaged **G** tensors at both the remote and MI regions are detailed in the Appendix.

## 5. Discussion

To the best of our knowledge, this has been the first time that growth tensor is quantitatively analysed from the human studies post-MI. It is challenging to measure growth tensors in situ from animal studies [26, 49], but more so from in vivo clinical studies. Imaging techniques can therefore provide an alternative source of information. For example, O'Regan et al. [40] quantified LV remodelling by tracking ventricular expansion using a 3D co-registration approach based on intensity-based similarities and in vivo cine and LGE images. However, the setbacks of tracking using intensity-based similarities are that these often suffer from varied imaging slice positions at different scan times, motion artefacts, signal intensity heterogeneity, as well as missing data between different slices. In this study, we adopt a different approach compared to O'Regan et al. [40]. Our LV geometries are first reconstructed by wraping a template mesh. Alignments along the long-axis (assuming the

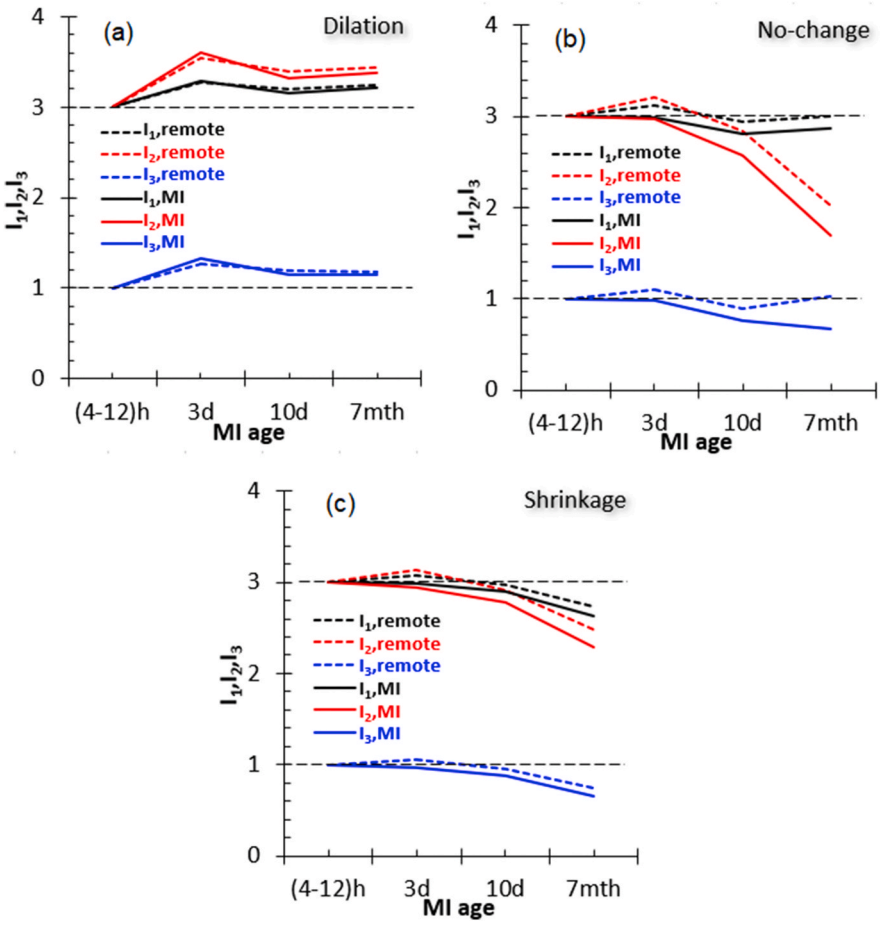


**Fig. 15.** The invariants of the growth tensor **G**: $I_1$ , $I_2$ and $I_3$ at 10-day and 7-month post-MI of the Dilation, No-Change and Shrinkage groups, respectively, error bars are not shown, standard deviations of the bars have been included in Table 5.

distance from the basal plane to the mitral annulus ring stays the same in one patient) and the circumferential direction (matching the two inferior right ventricular insertion points at the basal plane) are then performed to co-register 4 different LV geometries of the same patient. In this manner, the local shape changes or the apparent growth tensors can be more reliably estimated.

The LV geometry is described in a prolate spheroidal coordinate system by fitting to the segmented endocardial and epicardial boundaries using cubic B-Splines, and then a dense FE mesh is generated for calculating growth tensors. This is different from a few previous studies where a cubic Hermite interpolation was used with 16 FE patches to generate the smooth endo- and epi-surfaces [38,50,53]. Manual segmentation of cine and LGE images and motion corrections, which are time-consuming and require experienced users, have been used in this study. This limits its application to a large cohort of patient studies. Further development shall automate this process, for example, by adopting the machine learning approaches [31] for ventricular wall segmentation [4,14], geometry reconstructions [43]. Including both the left and right ventricles would provide more geometrical features for tracking growth tensors, however, automatically reconstructing the bi-ventricular geometry from in vivo cine CMR images remains challenging.

A few dimensionless parameters such as normalized LVEDV, mean growth tensor components and invariants are used to characterize the G&R process post-MI. The growth tensor components in the MI region are compared with experimental data of an ovine LV, and both qualitative and quantitative agreements are observed. Similar to the experiments, our study also shows that the growth tensor is diagonally dominated, either in the circumferential-transmural-longitudinal directions or via a transformation, the fibre-sheet-normal directions. Patients are further divided into three groups based on ±12% change in LVEDV. Our analysis using growth tensor components of the LV wall also supports this classification. In particular, we found that in both the Dilation and Shrinkage groups, the MI and remote regions have similar trends, and the wall-thinning is seen in all groups, but the increase/decrease in $G_{\mathrm{ff}}$ and $G_{\mathrm{nn}}$ are present in the Dilation/Shrinkage groups. In the No-Change group, the increase of $G_{\mathrm{ff}}$ and $G_{\mathrm{nn}}$ only occurs in the MI region, little variations are seen in $G_{\mathrm{ff}}$ and $G_{\mathrm{nn}}$ in the remote region. Hence the overall wall volume changes little after 7 months. 3D results also demonstrate severe shape change in the Dilation group. It suggests that local shape analysis can be a useful tool in quantifying the G&R process of this group.

Our observation on the Dilation group agrees with the previous ones [22,27]. In the first 7 days after MI, the LV dilates and the infarct zone expands, and later the infarct zone shrinks and LV wall thinning follows. For the Shrinkage and No-Change group, wall-thinning is always present and the MI size decreases. However, the LV itself doesn't dilate.

There is no between-group difference in the G&R parameters at 3 days post-MI. However, there is a between-group difference at 10 days onwards in the growth tensor component $G_{\mathrm{rr}}$ (Table 5), the invariants $I_1$, $I_2$, $I_3$ and $V_w/V_{w0}$, which can predict adverse and reverse modelling at 7 months post-MI. Except LVEF, most of the clinical indices in Table 2 are not related to the group differences even at 7 months post-MI. This shows that the apparent growth tensor could be more effective in providing statistically useful information for the prognosis of MI.

Our analysis is based on limited sample size, therefore the statistical significance of the results should be interpreted with caution. In addition, the growth tensor estimated from this work is not the true growth

**Table 5**
Average G&R for each group along the circumferential, longitudinal and radial directions at three time-points post-MI.

| | Location | No-Change | Dilation | Shrinkage | Dilation vs Shrinkage |
|---|---|---|---|---|---|
| | | (N = 2) | (N = 5) | (N = 8) | (p value) |
| **3 days** post reperfusion | | | | | |
| $G_{cc}$ | Remote | 0.9776±0.0140 | 0.9883±0.0456 | 1.0073±0.0444 | 0.237 |
| | MI | 0.9791±0.0065 | 0.9757±0.0544 | 1.0119±0.0486 | 0.126 |
| $G_{ll}$ | Remote | 0.9804±0.0504 | 1.0055±0.0322 | 1.0256±0.0653 | 0.558 |
| | MI | 0.9830±0.0504 | 1.0017±0.0366 | 1.0254±0.0716 | 0.214 |
| $G_{rr}$ | Remote | 1.0715±0.0099 | 1.0070±0.0899 | 1.0564±0.0659 | 0.161 |
| | MI | 1.0165±0.0592 | 0.9856±0.0640 | 1.0618±0.1397 | 0.094 |
| **10 days** post reperfusion | | | | | |
| $G_{cc}$ | Remote | 0.9805±0.0059 | 0.9979±0.0522 | 1.0162±0.0312 | 0.250 |
| | MI | 0.9922±0.0072 | 0.9661±0.0904 | 1.0204±0.0432 | 0.126 |
| $G_{ll}$ | Remote | 0.9848±0.0400 | 1.0093±0.0362 | 1.0263±0.0658 | 0.130 |
| | MI | 0.9954±0.0448 | 1.0064±0.0426 | 1.0245±0.0776 | 0.292 |
| $G_{rr}$ | Remote | 1.0740±0.2118 | 0.9368±0.0506 | 1.0276±0.0750 | 0.010 ($p$ <0.05) |
| | MI | 0.8903±0.2034 | 0.9462±0.0740 | 1.0107±0.0880 | 0.088 |
| **7 months** post reperfusion | | | | | |
| $G_{cc}$ | Remote | 0.9661±0.0101 | 0.9688±0.0146 | 1.0544±0.0526 | $5.05 \times 10^{-4}$ ($p$ <0.05) |
| | MI | 1.0673±0.0500 | 0.9188±0.0317 | 1.0498±0.0545 | $5.07 \times 10^{-5}$ ($p$ <0.05) |
| $G_{ll}$ | Remote | 1.0093±0.0263 | 0.9326±0.0290 | 1.0633±0.0685 | $1.62 \times 10^{-4}$ ($p$ <0.05) |
| | MI | 1.0587±0.0384 | 0.9165±0.0395 | 1.0683±0.0701 | $1.14 \times 10^{-4}$ ($p$ <0.05) |
| $G_{rr}$ | Remote | 1.0096±0.0275 | 0.9348±0.0506 | 0.9484±0.1175 | 0.410 |
| | MI | 0.7749±0.0801 | 0.9502±0.0782 | 0.9413±0.1069 | 0.105 |
| **3 days** post reperfusion | | | | | |
| $I_1$ | Remote | 3.1149±0.1486 | 3.0782±0.2752 | 3.2671±0.1966 | 0.112 |
| | MI | 2.9883±0.2181 | 2.9810±0.2004 | 3.2797±0.4771 | 0.064 |
| $I_2$ | Remote | 3.2082±0.3127 | 3.1388±0.5443 | 3.5360±0.4343 | 0.112 |
| | MI | 2.9771±0.4120 | 2.9431±0.3948 | 3.5974±1.1446 | 0.074 |
| $I_3$ | Remote | 1.0952±0.1617 | 1.2713±0.2447 | 1.0607±0.2685 | 0.092 |
| | MI | 0.9887±0.1945 | 1.3250±0.6882 | 0.9619±0.1948 | 0.085 |
| **10 days** post reperfusion | | | | | |
| $I_1$ | Remote | 3.1699±0.3952 | 2.9684±0.1884 | 3.2018±0.1582 | 0.026 ($p$ <0.05) |
| | MI | 2.8149±0.2931 | 2.8993±0.2621 | 3.1593±0.2374 | 0.052 |
| $I_2$ | Remote | 3.2811±0.7322 | 2.9195±0.3963 | 3.3883±0.3462 | 0.031 ($p$ <0.05) |
| | MI | 2.6227±0.6039 | 2.7801±0.4926 | 3.3132±0.5021 | 0.043 ($p$ <0.05) |
| $I_3$ | Remote | 1.1146±0.3425 | 1.1870±0.1888 | 0.9499±0.2059 | 0.033 ($p$ <0.05) |
| | MI | 0.8075±0.3100 | 1.1537±0.2648 | 0.8778±0.2268 | 0.034 ($p$ <0.05) |
| **7 months** post reperfusion | | | | | |
| $I_1$ | Remote | 3.0453±0.0844 | 2.7392±0.2039 | 3.2424±0.2008 | 0.001 ($p$ <0.05) |
| | MI | 2.9036±0.1651 | 2.6276±0.1690 | 3.2105±0.1920 | $1.17 \times 10^{-4}$ ($p$ <0.05) |
| $I_2$ | Remote | 3.0209±0.1643 | 2.4859±0.3818 | 3.4440±0.4437 | $8.56 \times 10^{-4}$ ($p$ <0.05) |
| | MI | 2.7069±0.3473 | 2.900±0.2984 | 3.3793±0.4058 | $6.58 \times 10^{-5}$ ($p$ <0.05) |
| $I_3$ | Remote | 0.9744±0.0810 | 0.7449±0.1823 | 1.1760±0.2648 | 0.002 ($p$ <0.05) |
| | MI | 0.7962±0.1777 | 1.1541±0.2223 | 0.6611±0.1330 | $1.13 \times 10^{-4}$ ($p$ <0.05) |

tensor as we discussed in section 2.3, but a convenient surrogate. Although the similar approximation has been adopted in the literature [40], and these data can be used in mathematical modelling of growth and remodelling, the careful manoeuvre will be required to remove the elastic deformations between the reference and loaded configurations.

Growth tensors should be estimated by tracking the same material point at different times. However, in this work, the correspondence is assumed according to the numbering system in the templated mesh. Two mesh nodes with the same number at different times after MI are not necessarily the same material points. This implies there may be multiple solutions to G&R. To alleviate this problem, we annotated the interventricular septum during LV segmentation, and generated the mesh separately in the septum and the remaining part. Then we could match the two right-ventricular insertions similar to the landmark-based registration. Consequently, the nodes with the same number at different times are more likely to be the same material points. We remark that other approaches, such as the diffeomorphic mapping taking into account both the geometrical features and image characteristics [8], or shape mode variations extracted from certain dimension reduction techniques [37], could provide more accurate results for determining the material point correspondence, but are more complex.

Although techniques such as diffusion tensor MRI have the potential to acquire in vivo myofibre structure [13,29,32,36], these are not routinely available on clinical MRI scanners. Hence, we used a rule-based fibre structure for all the patients. However, by perturbing the chosen fibre structure within the physiological range, we found that

results do not change qualitatively. Finally, it is worth mentioning that the co-registration among different LV geometries is not a well-posed problem. Either image tracking [40] or geometry matching may not reproduce all the local myocardium changes. Introducing mechanistic G&R models may improve the growth tensor estimation, but remains a future research topic since it requires much more clinical and in vitro measurements at both macroscopic and microscopic levels.

## 6. Conclusion

In this paper, we have developed an image-derived method for estimating apparent myocardial growth tensors in 16 patients post-MI. Both routinely available cine and LGE CMR images are used for personalized LV geometry reconstruction. We have demonstrated that the estimated growth tensor agrees well with published experimental data and conventional clinical observation. Our results show that the greatest shape change occurs in the Dilation group and the least in the Shrinkage group. Both $G_{\mathrm{ff}}$ and $G_{\mathrm{nn}}$ are greater than 1 in the Dilation group (adverse remodelling) with $G_{\mathrm{ss}}$ below 1, indicating elongation of myocytes and wall-thinning due to extracellular matrix degradation and myocyte apoptosis. Different G&R patterns are identified in the Shrinkage group (reverse remodelling), in which both $G_{\mathrm{ff}}$ and $G_{\mathrm{nn}}$ are less than 1. Wall-thinning occurs in all patients, but the wall volume change, as indicated by $I_3$, is found to increase/decrease at 7 months post-MI in the Dilation/Shrinkage groups both in the MI and remote regions. Interestingly, although the No-Change group has "no change" (change less than 12%) in the LV volume, there are significant and competing changes inside the LV wall along the fibre-sheet-normal directions, and these changes are also different in the MI and remote regions. We further show that the growth tensor invariants at 10-day and 7-month post-MI are significantly different between the Dilation group and the Shrinkage group, and they seem to have stronger explanatory power for identifying adverse and reverse remodelling patients compared to clinical indices, i.e. MVO extent and MI size, etc. The clinical and prognostic significance of the growth tensor invariants merits further study. Although with limited sample size, our growth tensor estimation for different G&R groups provides a starting point for in-depth mechanistically understanding of growth and remodelling in the human heart following an acute-MI. Further research is warranted, both in terms of sample size and multicentre study design.

## Funding

This project is funded by the UK Engineering and Physical Sciences Research Council grants (EP/S020950, EP/S014284/1, EP/S030875, and EP/N014642).. KM and CB were also supported by grants from the British Heart Foundation (PG/11/228474; PG/14/64/31043; FS/15/54/31639; CoE/RE/18/6134217).

## Data availability statement

All quantities including the growth tensor estimated for all 16 patients are made available through the Supplemental Data.

## CRediT authorship contribution statement

**Wenguang Li:** Segmentation, Reconstruction, Software, improvement, Data curation, Result analysis, Writing - original draft. **Hao Gao:** Methodology, Software, Data curation, Critical reviewing. **Kenneth Mangion:** Data curation, Clinical analysis, Critical reviewing. **Colin Berry:** Data curation, Clinical analysis, Critical reviewing. **Xiaoyu Luo:** Conceptualization, of this study, Result analysis, Critical reviewing.

## Declaration of competing interest

The authors declare that they have no known competing financial interests or personal relationships that could have appeared to influence the work reported in this paper.

## Acknowledgements

We would like to thank Prof. Ray Ogden for helpful discussions.

## Appendix

The group and region-averaged **G** components for the Dilation group:

$$
\begin{aligned}
\mathbf{G}^{\mathrm{remote}}_{clr\_10d} &= \begin{bmatrix} 1.0162 \pm 0.0756 & 0.0015 \pm 0.0122 & -0.0013 \pm 0.0255 \\ 0.0001 \pm 0.0198 & 1.0263 \pm 0.0424 & 0.0025 \pm 0.0358 \\ 0.0056 \pm 0.1120 & -0.0084 \pm 0.0993 & 1.0276 \pm 0.1397 \end{bmatrix} \\
\mathbf{G}^{\mathrm{MI}}_{clr\_10d} &= \begin{bmatrix} 1.0204 \pm 0.0539 & 0.0017 \pm 0.0084 & -0.0008 \pm 0.0136 \\ 0.0024 \pm 0.0092 & 1.0245 \pm 0.0237 & -0.0012 \pm 0.0307 \\ 0.0009 \pm 0.0718 & -0.0034 \pm 0.0785 & 1.0107 \pm 0.1245 \end{bmatrix} \\
\mathbf{G}^{\mathrm{remote}}_{clr\_7mth} &= \begin{bmatrix} 1.0544 \pm 0.1022 & 0.0013 \pm 0.0150 & -0.0010 \pm 0.0260 \\ -0.0008 \pm 0.0252 & 1.0633 \pm 0.0466 & 0.0079 \pm 0.0362 \\ 0.0031 \pm 0.1486 & -0.0085 \pm 0.1268 & 0.9484 \pm 0.1381 \end{bmatrix} \\
\mathbf{G}^{\mathrm{MI}}_{clr\_7mth} &= \begin{bmatrix} 1.0498 \pm 0.0725 & 0.0033 \pm 0.0116 & 0.0019 \pm 0.0168 \\ 0.0008 \pm 0.0156 & 1.0683 \pm 0.0308 & 0.0027 \pm 0.0299 \\ 0.0363 \pm 0.1013 & -0.0235 \pm 0.0959 & 0.9413 \pm 0.1249 \end{bmatrix}.
\end{aligned}
\tag{13}
$$

in which crl represents the circumferential-radial-longitudinal coordinate system.

Similarly, the group and region-averaged **G** components for the No-Change group:

$$
\begin{aligned}
\mathbf{G}^{\text{remote}}_{clr\_10d} &= \begin{bmatrix} 0.9805 \pm 0.0491 & -0.0019 \pm 0.0086 & 0.0051 \pm 0.0197 \\ -0.0012 \pm 0.0112 & 0.9848 \pm 0.0298 & 0.0081 \pm 0.0293 \\ 0.0002 \pm 0.0740 & 0.0236 \pm 0.0806 & 1.0740 \pm 0.2118 \end{bmatrix} \\
\mathbf{G}^{\text{MI}}_{clr\_10d} &= \begin{bmatrix} 0.9922 \pm 0.0387 & 0.0001 \pm 0.0041 & 0.0015 \pm 0.0090 \\ 0.0014 \pm 0.0067 & 0.9954 \pm 0.0134 & 0.0017 \pm 0.0267 \\ -0.0161 \pm 0.0473 & -0.0069 \pm 0.0814 & 0.8903 \pm 0.1041 \end{bmatrix} \\
\mathbf{G}^{\text{remote}}_{clr\_7mth} &= \begin{bmatrix} 0.9661 \pm 0.0906 & -0.0052 \pm 0.0115 & -0.0015 \pm 0.0289 \\ -0.0063 \pm 0.0221 & 1.0093 \pm 0.0495 & 0.0301 \pm 0.0328 \\ -0.0106 \pm 0.1329 & 0.0141 \pm 0.1014 & 1.0096 \pm 0.1727 \end{bmatrix} \\
\mathbf{G}^{\text{MI}}_{clr\_7mth} &= \begin{bmatrix} 1.0673 \pm 0.0577 & 0.0018 \pm 0.0050 & 0.0065 \pm 0.0154 \\ -0.0041 \pm 0.0149 & 1.0587 \pm 0.0219 & 0.0044 \pm 0.0223 \\ 0.0418 \pm 0.0777 & -0.0504 \pm 0.0850 & 0.7749 \pm 0.1020 \end{bmatrix}.
\end{aligned} \tag{14}
$$

And the group and region-averaged **G** components for the Shrinkage group:

$$
\begin{aligned}
\mathbf{G}^{\text{remote}}_{clr\_10d} &= \begin{bmatrix} 0.9979 \pm 0.0918 & -0.0013 \pm 0.0121 & -0.0010 \pm 0.0224 \\ -0.0033 \pm 0.0178 & 1.0093 \pm 0.0357 & 0.0083 \pm 0.0336 \\ 0.0071 \pm 0.1402 & 0.0011 \pm 0.0995 & 0.9368 \pm 0.1487 \end{bmatrix} \\
\mathbf{G}^{\text{MI}}_{clr\_10d} &= \begin{bmatrix} 0.9661 \pm 0.0654 & -0.0056 \pm 0.0101 & -0.0085 \pm 0.0184 \\ -0.0037 \pm 0.0117 & 1.0064 \pm 0.0207 & 0.0073 \pm 0.0236 \\ -0.0320 \pm 0.1010 & -0.0099 \pm 0.0740 & 0.9462 \pm 0.1226 \end{bmatrix} \\
\mathbf{G}^{\text{remote}}_{clr\_7mth} &= \begin{bmatrix} 0.9688 \pm 0.0768 & -0.0006 \pm 0.0115 & -0.0004 \pm 0.0187 \\ -0.0003 \pm 0.0167 & 0.9326 \pm 0.0358 & -0.0111 \pm 0.0265 \\ 0.0008 \pm 0.1073 & 0.0093 \pm 0.0963 & 0.9348 \pm 0.1180 \end{bmatrix} \\
\mathbf{G}^{\text{MI}}_{clr\_7mth} &= \begin{bmatrix} 0.9188 \pm 0.0563 & 0.0010 \pm 0.0088 & 0.0005 \pm 0.0132 \\ -0.0010 \pm 0.0098 & 0.9165 \pm 0.0192 & -0.0021 \pm 0.0183 \\ 0.0027 \pm 0.0750 & 0.0082 \pm 0.0788 & 0.9502 \pm 0.0973 \end{bmatrix}.
\end{aligned} \tag{15}
$$

## Appendix A. Supplementary data

Supplementary data to this article can be found online at https://doi.org/10.1016/j.compbiomed.2020.104168.

## References


[1] D. Ambrosi, M. Ben Amar, C.J. Cyron, et al., Growth and remodelling of living tissues: perspectives, challenges and opportunities, J. R. Soc. Interface 16 (2019) 20190233, https://doi.org/10.1098/rsif.2019.0233. https://royalsocietypublishing.org/doi/10.1098/rsif.2019.0233.

[2] S. Ardekani, R.G. Weiss, A.C. Lardo, et al., Computational method for identifying and quantifying shape features of human left ventricular remodeling, Ann. Biomed. Eng. 37 (2009) 1043–1054.

[3] J. Arumugam, J. Mojumder, G. Kassab, et al., Model of anisotropic reverse cardiac growth in mechanical dyssynchronyn, Sci. Rep. 9 (2019), https://doi.org/10.1038/s41598-019-48670-8.

[4] W. Bai, M. Sinclair, G. Tarroni, et al., Automated cardiovascular magnetic resonance image analysis with fully convolutional networks, J. Cardiovasc. Magn. Reson. 20 (2018) 65.

[5] S.F. Baracho, D.J. Pinheiro, C.M. de Godoy, et al., A segmentation method for myocardial ischemia/infarction applicable in heart photos, Comput. Biol. Med. 87 (2017) 285–307.

[6] P. Beliveau, F. Cheriet, S.A. Anderson, et al., Quantitative assessment of myocardial fibrosis in an age-related rat model by ex vivo late gadolinium enhancement magnetic resonance imaging with histopathological correlation, Comput. Biol. Med. 65 (2015) 103–113.

[7] A.S. Bhatt, A.P. Ambrosy, E.J. Velazquez, Adverse remodeling and reverse remodeling after myocardial infarction, Curr. Cardiol. Rep. 19 (2017) 71.

[8] A. Bône, O. Colliot, S. Durrleman, Learning distributions of shape trajectories from longitudinal datasets: a hierarchical model on a manifold of diffeomorphisms, in: Proceedings of the IEEE Conference on Computer Vision and Pattern Recognition, 2018, pp. 9271–9280.

[9] P.H. Bovendeerd, Modeling of cardiac growth and remodeling of myofiber orientation, J. Biomech. 45 (2012) 872–881.

[10] H. Bulluck, R. Dharmakumar, A.E. Arai, et al., Cardiovascular magnetic resonance in acute st-segment–elevation myocardial infarction: recent advances, controversies, and future directions, Circulation 137 (2018) 1949–1964.

[11] H. Bulluck, Y.Y. Go, G. Crimi, et al., Defining left ventricular remodeling following acute ST-segment elevation myocardial infarction using cardiovascular magnetic resonance, J. Cardiovasc. Magn. Reson. 19 (2017) 26.

[12] D. Carrick, K.G. Oldroyd, M. McEntegart, et al., A randomized trial of deferred stenting versus immediate stenting to prevent no-or slow-reflow in acute st-segment elevation myocardial infarction (defer-stemi), J. Am. Coll. Cardiol. 63 (2014) 2088–2098.

[13] J. Chen, S.K. Song, W. Liu, et al., Remodeling of cardiac fiber structure after infarction in rats quantified with diffusion tensor mri, Am. J. Physiol. Heart Circ. Physiol. 285 (2003) H946–H954.

[14] J. Duan, G. Bello, J. Schlemper, et al., Automatic 3d bi-ventricular segmentation of cardiac images by a shape-refined multi-task deep learning approach, IEEE Trans. Med. Imag. 38 (2019) 2151–2164.

[15] D.S. Fieno, R.J. Kim, E.L. Chen, et al., Contrast-enhanced magnetic resonance imaging of myocardium at risk: distinction between reversible and irreversible injury throughout infarct healing, J. Am. Coll. Cardiol. 36 (2000) 1985–1991.

[16] B.A. French, C.M. Kramer, Mechanisms of post-infarct left ventricular remodeling, Drug Discov. Today Dis. Mech. 4 (2007) 185–196.

[17] J.J. Gajarsa, R.A. Kloner, Left ventricular remodeling in the post-infarction heart: a review of cellular, molecular mechanisms, and therapeutic modalities, Heart Fail. Rev. 16 (2011) 13–21.

[18] H. Gao, A. Aderhold, K. Mangion, et al., Changes and classification in myocardial contractile function in the left ventricle following acute myocardial infarction, J. R. Soc. Interface 14 (2017) 20170203.

[19] H. Gao, A. Allan, C. McComb, et al., Left ventricular strain and its pattern estimated from cine CMR and validation with DENSE, Phys. Med. Biol. 59 (2014) 3637–3656.

[20] H. Gao, D. Carrick, C. Berry, et al., Dynamic finite-strain modelling of the human left ventricle in health and disease using an immersed boundary-finite element method, IMA J. Appl. Math. 79 (2014) 978–1010.

[21] H. Gao, W. Li, L. Cai, et al., Parameter estimation in a Holzapfel–Ogden law for healthy myocardium, J. Eng. Math. 95 (2015) 231–248, https://doi.org/10.1007/s10665-014-9740-3. http://link.springer.com/10.1007/s10665-014-9740-3.

[22] P. Gaudron, C. Eilles, G. Ertl, et al., Early remodelling of the left ventricle in patients with myocardial infarction, Eur. Heart J. 11 (1990) 139–146.

[23] S. Goktepe, O.J. Abilez, K.K. Parker, et al., A multiscale model for eccentric and concentric cardiac growth through sarcomerogenesis, J. Theor. Biol. 265 (2010) 433–442.

[24] W. Grossman, D. Jones, L.P. McLaurin, Wall stress and patterns of hypertrophy in the human left ventricle, J. Clin. Invest. 56 (1975) 56–64.

[25] E. Heiberg, M. Ugander, H. Engblom, et al., Automated quantification of myocardial infarction from mr images by accounting for partial volume effects: animal, phantom, and human study, Radiology 246 (2008) 581–588.
[26] J.W. Holmes, H. Yamashita, L.K. Waldman, et al., Scar remodeling and transmural deformation after infarction in the pig, Circulation 90 (1994) 411–420.
[27] D.A. Kass, W.L. Maughan, A. Ciuffo, et al., Disproportionate epicardial dilation after transmural infarction of the canine left ventricle: acute and chronic differences, J. Am. Coll. Cardiol. 11 (1988) 177–185.
[28] W. Kroon, T. Delhaas, T. Arts, et al., Computational modeling of volumetric soft tissue growth: application to the cardiac left ventricle, Biomech. Model. Mechanobiol. 8 (2008) 301–309.
[29] G.L. Kung, M. Vaseghi, J.K.J. Gahm, et al., Microstructural infarct border zone remodeling in the post-infarct swine heart measured by diffusion tensor mri, Front. Physiol. 9 (2018), https://doi.org/10.3389/fphys.2018.00826.
[30] L.C. Lee, G.S. Kassab, J.M. Guccione, Mathematical modeling of cardiac growth and remodeling, Wiley Interdiscipl. Rev. Syst. Biol. Med. 8 (2016) 211–226.
[31] T. Leiner, D. Rueckert, A. Suinesiaputra, et al., Machine learning in cardiovascular magnetic resonance: basic concepts and applications, J. Cardiovasc. Magn. Reson. 21 (2019) 1–14.
[32] D.G. Leon, M. Lopez-Yunta, J.M. Alfonso-Almazan, et al., Three-dimensional cardiac fibre disorganization as a novel parameter for ventricular arrhythmia stratification after myocardial infarction, Europace 21 (2019) 822–832.
[33] W. Li, A. Lazarus, H. Gao, et al., Analysis of cardiac amyloidosis progression using model-based markers, Front. Physiol. 11 (2020) 324, https://doi.org/10.3389/fphys.2020.00324. https://www.frontiersin.org/article/10.3389/fphys.2020.00324/full.
[34] Y. Liu, H. Wen, R.C. Gorman, et al., Reconstruction of myocardial tissue motion and strain fields from displacement-encoded mr imaging, Am. J. Physiol. Heart Circ. Physiol. 297 (2009) H1151–H1162.
[35] P. Madhav, V. Mai, M. Zhang, et al., An automated segmentation method for assessing myocardial infarct size using k-means algorithm, Proc. Int. Soc. Mag. Reson. Med. (2003) 945.
[36] C. Mekkaoui, M.P. Jackwski, W.J. Kozerke, et al., Myocardial scar delineation using diffusion tensor magnetic resonance tractography, J. Am. Heart Assoc. 7 (2019), https://doi.org/10.1161/JAHA.117.007834.
[37] H.K. Narayan, R. Xu, N. Forsch, et al., Atlas-based measures of left ventricular shape may improve characterization of adverse remodeling in anthracycline-exposed childhood cancer survivors: a cross-sectional imaging study, Cardio-Oncol. 6 (2020) 1–9.
[38] P.M. Nielsen, I.J. Le Grice, B.H. Smaill, et al., Mathematical model of geometry and fibrous structure of the heart, Am. J. Physiol. Heart Circ. Physiol. 260 (1991) H1365–H1378.
[39] J.H. Omens, J.W. Covell, Transmural distribution of myocardial tissue growth induced by volume-overload hypertrophy in the dog, Circulation 84 (1991) 1235–1245.
[40] D. O'Regan, W. Shi, B. Ariff, et al., Remodeling after acute myocardial infarction: mapping ventricular dilatation using three dimensional cmr image registration, J. Cardiovasc. Magn. Reson. 14 (2012), https://doi.org/10.1186/1532-429X-14-41.
[41] E.K. Rodriguez, A. Hoger, A.D. McCulloch, Stress-dependent finite growth in soft elastic tissues, J. Biomech. 27 (1994) 455–467.
[42] V.L. Roger, Epidemiology of heart failure, Circ. Res. 113 (2013) 646–659.
[43] L. Romaszko, A. Borowska, A. Lazarus, et al., Direct learning left ventricular meshes from CMR images, in: International Conference on Statistics: Theory and Applications, Lisbon, Portugal, August 13 - 14, 2019.
[44] J. Schulz-Menger, D.A. Bluemke, J. Bremerich, et al., Standardized image interpretation and post processing in cardiovascular magnetic resonance: society for cardiovascular magnetic resonance (scmr) board of trustees task force on standardized post processing, J. Cardiovasc. Magn. Reson. 15 (2013) 35, https://doi.org/10.1186/1532-429X-15-35.
[45] V.K. Sudarshan, U.R. Acharya, E.Y. Ng, et al., Data mining framework for identification of myocardial infarction stages in ultrasound: a hybrid feature extraction paradigm (part 2), Comput. Biol. Med. 71 (2016) 241–251.
[46] V.K. Sudarshan, E.Y. Ng, U.R. Acharya, et al., Computer-aided diagnosis of myocardial infarction using ultrasound images with dwt, glcm and hos methods: a comparative study, Comput. Biol. Med. 62 (2015) 86–93.
[47] M.G. Sutton, N. Sharpe, Left ventricular remodeling after myocardial infarction: pathophysiology and therapy, Circulation 101 (2000) 2981–2988.
[48] L.A. Taber, Biomechanics of growth, remodeling, and morphogenesis, Appl. Mech. Rev. 48 (1995) 487–545.
[49] A. Tsamis, A. Cheng, T.C. Nguyen, et al., Kinematics of cardiac growth: in vivo characterization of growth tensors and strains, J. Mech. Behav. Biomed. Mater. 8 (2012) 165–177.
[50] T.P. Usyk, A.D. McCulloch, Computational methods for soft tissue biomechanics, in: Biomechanics of Soft Tissue in Cardiovascular Systems, Springer, 2003, pp. 273–342.
[51] R.S. Valagaleti, M.J. Pencina, J.M. Murabito, et al., Long-term trends in the incidence of heart failure sfter myocardial infarction, Circulation 118 (2008) 2057–2062.
[52] H.M. Wang, H. Gao, X.Y. Luo, et al., Structure-based finite strain modelling of the human left ventricle in diastole, Int. J. Numerical Methods Biomed. Eng. 29 (2013) 83–103.
[53] A.A. Young, C.M. Kramer, V.A. Ferrari, et al., Three-dimensional left ventricular deformation in hypertrophic cardiomyopathy, Circulation 90 (1994) 854–867.
[54] H. Yousefi-Banaem, S. Kermani, S. Asiaei, et al., Prediction of myocardial infarction by assessing regional cardiac wall in cmr images through active mesh modelings, Comput. Biol. Med. 80 (2017) 56–64.
[55] X. Zhang, B.R. Cowan, D.A. Bluemke, et al., Atlas-based quantification of cardiac remodeling due to myocardial infarction, PloS One 9 (2014), e110243.
[56] X. Zhuan, X.Y. Luo, H. Gao, et al., Coupled agent-based and hyperelastic modelling of the left ventricle post-myocardial infarction, Int. J. Numerical Methods Biomed. Eng. 35 (2019) e3155.